

# Assimilation of GPS Refractivity from FORMOSAT-3/COSMIC Using a Nonlocal Operator with WRF 3DVAR and Its Impact on the Prediction of a Typhoon Event

Shu-Ya Chen<sup>1</sup>, Ching-Yuang Huang<sup>1,\*</sup>, Ying-Hwa Kuo<sup>2,3</sup>,  
Yong-Run Guo<sup>3</sup>, and Sergey Sokolovskiy<sup>2</sup>

<sup>1</sup>Department of Atmospheric Sciences, National Central University, Chung-Li, Taiwan, ROC

<sup>2</sup>University Corporation for Atmospheric Research, Boulder, Colorado, USA

<sup>3</sup>National Center for Atmospheric Research, Boulder, Colorado, USA

Received 27 June 2007, accepted 29 November 2007

---

## ABSTRACT

A nonlocal observation operator has been developed to assimilate GPS radio occultation (RO) refractivity with WRF 3DVAR. For simplicity, in the past GPS RO refractivity was often assimilated using a local observation operator with the assumption that the GPS RO observation was representative of a model local point. Such an operator did not take into account the effects of horizontal inhomogeneity on the derived GPS RO refractivity. In order to more accurately model the observables, Sokolovskiy et al. (2005a) developed a nonlocal observation operator, which would take into account the effects of horizontal inhomogeneity on GPS RO measurements. This nonlocal observation operator calculates the integrated amount of the model refractivity along the ray paths centered at the perigee points. For comparative purposes, the nonlocal observation operator can be simplified by limiting the length of integration near the RO point. This is called the “local operator variant”, which is equivalent to the original local operator except that the original one is performed with fixed tangent points at observation levels. For computational efficiency, assimilation using both the nonlocal operator and local operator variant now is performed with smear tangent points at the mean height of each model vertical level. In this study, the statistics of observation errors using both local and nonlocal operators were estimated based on WRF simulations. The observation errors produced by the nonlocal operator are about two times smaller than those generated by the local operator and in agreement with Sokolovskiy et al. (2005b).

Each of the three operators is used to assimilate GPS RO refractivity soundings from the FORMOSAT-3/COSMIC mission using the WRF 3DVAR system. The WRF model then is applied to simulate Typhoons Kaemi (July 2006) which struck Taiwan with significant torrential rainfall. The analysis increments produced by the nonlocal operator and local operator variant are quite similar in horizontal and vertical distributions; whereas, the former is slightly stretched along the ray’s direction, as a result of the longer integration length. The simulated typhoon tracks prior to landfall are quite similar for the three operators. Both the nonlocal operator and local operator variant improve the detoured track after landfall as predicted by the local operator. The nonlocal operator outperforms the two local operators in rainfall prediction at later times. The performances of the nonlocal operator in general are promising and can replace the local operator at no marked cost of computational efficiency.

Key words: FORMOSAT-3/COSMIC, Data assimilation, Typhoon

Citation: Chen, S. Y., C. Y. Huang, Y. H. Kuo, Y. R. Guo, and S. Sokolovskiy, 2009: Assimilation of GPS refractivity from FORMOSAT-3/COSMIC using a nonlocal operator with WRF 3DVAR and its impact on the prediction of a typhoon event. *Terr. Atmos. Ocean. Sci.*, 20, 133-154, doi: 10.3319/TAO.2007.11.29.01(F3C)

---

## 1. INTRODUCTION

Remote sensing using about 28 Global Positioning System (GPS) satellites in current operating may be effectively

carried out by receiving GPS signals with airborne or ground-based receivers. The radio rays are bent when traversing the atmosphere. Received by Low-Earth Orbit (LEO) satellites, radio occultation (RO) signals provide useful information about the state of the atmosphere. Con-

---

\* Corresponding author  
E-mail: hcy@atm.ncu.edu.tw

structing a global constellation network through such radio occultation and mobile LEO satellites, in particular, have several advantages such as a high vertical resolution, no need for calibration, unaffected by cloud cover or rainfall, and global coverage (Anthes et al. 2000). The comparisons of GPS RO observations with conventional radiosonde soundings were conducted in a number of studies (e.g., Rocken et al. 1997; Kuo et al. 2004, 2005). In the middle and upper troposphere, the accuracy of the refractivity retrieved from GPS RO soundings is compatible to or higher than that of radiosondes as reported by Kuo et al. (2005).

Depending on the level of data processing, various variables can be retrieved from GPS RO observations for use in data assimilation, ranging from raw excess phases to retrieved moisture and/or temperature profiles (see Kuo et al. 2000, 2004). The bending angle, defined as the angle between the incident ray and the outgoing ray (Kursinsky et al. 2000), can be retrieved from low-level data with the assumption of spherical symmetry. After applying the Abel inversion for bending angles, GPS RO refractivity profiles can be obtained at an occultation point as an intermediate product with presumed local spherical symmetry. There are several impact studies using GPS RO refractivity soundings (Kuo et al. 2004, 2005; Huang et al. 2005; Chen et al. 2006; Cucurull et al. 2006). For example, Huang et al. (2005) assimilated several GPS RO refractivity soundings into the fifth-generation Pennsylvania State University National Center for Atmospheric Research Mesoscale Model (MM5) with a three-dimensional variational data assimilation system (3DVAR) and showed that both tracking and accumulated rainfall predictions were improved in simulating two typhoons which struck Taiwan, Nari (2001) and Nakri (2002). Data assimilation studies have shown that GPS RO bending angles and refractivities can have a positive impact on regional as well as global weather predictions (Kuo et al. 1997; Zou et al. 1999, 2000; Liu and Zou 2003; Healy et al. 2005; Huang et al. 2005; Cucurull et al. 2006; Healy and Thepaut 2006).

The atmospheric refractivity ( $N$ ) is related to several meteorological variables, such as

$$N = 77.6 \frac{P}{T} + 3.73 \times 10^5 \frac{P_w}{T^2} \quad (1)$$

where  $P_w$  is water vapor pressure in hPa,  $T$  air temperature in K, and  $P$  the pressure of the atmosphere in hPa, as the model predicted variables vary with height. As mentioned above, assimilation of the Abel-retrieved refractivity profiles has assumed local measurement at the perigee point where the GPS ray is closest to the earth. This treatment also indicates that the observed refractivity is modeled as local refractivity when assimilated by a local refractivity operator; however, this results in certain representative errors due to the characteristics of the Abel-retrieved re-

fractivity that accounts for an integrated amount of refractivity along the path of the ray in a spherically-symmetric atmosphere (Poli 2004; Poli and Joiner 2004; Sokolovskiy et al. 2005a, b). In order to take into account the effect of the integration, Sokolovskiy et al. (2005a, b) suggest the use of *excess phase* as the observable for assimilation, which is defined as the integrated amount of refractivity along a ray. For simplicity and efficiency, the ray of the integration can be assumed as a straight line (for details see Fig. 1 of Sokolovskiy et al. 2005b). Such a forward model is the so-called nonlocal operator as compared to the local operator using the point refractivity. Sokolovskiy et al. (2005a, b) found that the observational errors produced by the nonlocal operator are smaller than those by the local operator, which decreases by a factor 1.5 to 2 below 6 km. This error reduction is considerable in the case of strong horizontal moisture and temperature gradients. For the nonlocal and local operators, we also estimated their observation errors in our simulated domain in this study.

Observations and modeling studies indicate that the bending angle of a ray tangent to the surface may be only as large as 3 degrees (e.g., Zou et al. 1999; Healy and Thepaut 2006). Hence, it is reasonable to use a straight line to represent the actual ray, and such approximation will be cost-effective for our model assimilation. In this study, we develop just such a new operator to assimilate the excess phase to investigate the nonlocal effect along a straight ray path, and implement this operator into the 3DVAR for the Weather Research & Forecasting (WRF) Model (see section 2 for more descriptions).

The launch of six FORMOSAT-3/COSMIC (FORMOSA Satellite #3/Constellation Observing System for Meteorology, Ionosphere, and Climate) satellites on 15 April 2006 provides a great opportunity for a regional model to assimilate more GPS RO data than available before (see <http://www.cosmic.ucar.edu>). By August 2006, several significant typhoons struck Taiwan with a few of RO soundings from FORMOSAT-3/COSMIC within our simulation domain. We choose one of the typhoon events, Kaemi (July 2006) to illustrate the feasibility of the new operator. We will compare the results in more detail using both local and nonlocal operators in a simulation of Typhoon Kaemi, and discuss the possible impact of the GPS RO refractivity assimilation on typhoon tracking and rainfall prediction. A brief introduction of the methodology (including the observation error estimation, nonlocal operator, and the weather model) will be given in section 2. The design of the experiments and simulated results will be described in section 3 where the comparisons of model results with the observations will be focused on both typhoon track prediction and accumulated rainfalls over Taiwan. Several sensitivity tests and discussions are provided in section 4. Finally, we will offer our conclusions in section 5.

## 2. THE METHODOLOGIES

The updated WRF Model (version 2.1.2), which is a next-generation mesoscale numerical weather prediction system, was applied to simulate Typhoon Kaemi (2006). The details of the WRF model can be found on the web site (<http://wrf-model.org>) as well as in Skamarock et al. (2005). The model is compressible and non-hydrostatic, and thus is capable of depicting the convective systems associated with a typhoon. WRF features multiple dynamical cores with high-order numerics and allows for computational parallelism that can enhance numerical accuracy and efficiency. The WRF 3DVAR was developed based on the MM5 3DVAR, and they share the same observation operators (for details of the WRF/MM5 3DVAR, see Barker et al. 2003, 2004). By minimizing a cost function, which calculates the magnitude of differences between the analysis and observations, the ingested observations can be used to adjust the initial analysis through proper weighting depending on observation and background error statistics (Wu et al. 2002). In this study, we will use the WRF 3DVAR (version 2.1) with the nonlocal operator for assimilation of the GPS RO data.

### 2.1 Nonlocal Operator in WRF 3DVAR

In earlier studies, GPS RO refractivity has been assimilated by assuming that the retrieved refractivity is representative of a local value valid at the ray perigee point. Such an approach, though computationally efficient, does not take into consideration the effects of horizontal gradients on the retrieved GPS refractivity and will become associated with some errors of representativeness. Sokolovskiy et al. (2005a) show that such errors can become much more sizeable over regions with significant horizontal moisture or temperature gradients. In order to reduce the representativeness errors, a nonlocal operator is used to take into account the effect of horizontal gradients.

In this study, we developed a new assimilation operator for WRF 3DVAR. To account for nonlocal effects, local refractivity is integrated along the ray path which is approximated by a straight line and this integrated amount is treated as a new observable (excess phase) defined as  $S = \int N dl$  where  $l$  is the ray path (Sokolovskiy et al. 2005a, b). First of all, we obtained retrieved vertical profiles from the COSMIC Data Analysis and Archival Center (CDAAC), which include the longitude, latitude and height of a tangent point, the associated refractivity and the azimuth of an incoming ray. Then, we calculated the model mean heights by averaging the heights of all the model grids on each model vertical level. The above observations (including the positions of tangent points) were gotten on the model mean heights by a vertical average. We believe that such a vertical average may still retain enough signals from the observations

without going into details that the model cannot resolve. Since the operator is oriented efficiently with reasonable accuracy, the developed version fits our goals. The model variables were interpolated by a cubic spline into the model mean heights. Then, both observation and model refractivities were integrated along a ray path by a step size of 5 km for each tangent point. It is important to use the same approximation for calculation of the excess phase from the model and from an observation. This results in cancellation, to a major extent, of the errors arising from the straight-line approximation for rays. Herein, some properties of the nonlocal operator should be noted:

- (1) The assimilation is performed at model mean heights for saving computational time and also reducing the aliasing of high vertical resolution variations in the GPS refractivity observations onto the much lower vertical resolutions of the model.
- (2) Both observations and model refractivities are integrated using the same operator with two constraints that confine the ray within the model domain and cannot allow penetration through terrain.
- (3) The observed refractivity is assumed to be spherically symmetric about the RO point. The coordinates of the perigee point for each ray may vary with geodetic height.
- (4) The ray is presumed to be a straight line for simplicity and the integration is terminated before the ray has approached the model top which is set to 50 hPa (about 20 km in height).
- (5) The error statistics for the excess phase is idealized by an approximated function of the relative observation errors which are 1% in the lowest layer of 2 km and then decrease monotonically with height to about 0.2% at 10 km height (see below for further details).

The default local operator in WRF 3DVAR assimilates refractivity from CDAAC with fixed tangent points at observation heights by mapping model variables into the observation heights. Note that this is a discrepancy in the heights of assimilation between the local operator and the nonlocal operator. For accounting the smearing of tangent points, we also develop a local operator variant in the WRF 3DVAR to provide a direct evaluation of the effect of integration. The local operator variant differs from the nonlocal operator only in that no ray integration is performed.

### 2.2 Observation Errors

It is important to have consistent error statistics of observations for use in assimilation. Both local and nonlocal operators were used to assimilate the corresponding variables as observables. The apparent errors consist of two sources, one from the model itself and the other from the observations. First, the apparent error can be estimated by

calculating the differences between the forecast results and the observations. Then, we estimate the forecast errors following the method used by Hollingsworth and Lönnberg (1986). It is assumed that the observation errors are uncorrelated with each other, and they are also uncorrelated with the forecast errors. We estimated the correlated forecast errors using the 12-h forecast results of WRF model. The observation error thus can be obtained as  $\sigma_o^2$ ,  $\sigma_a^2$ ,  $\sigma_f^2$  as discussed in Kuo et al. (2004), where  $\sigma_o^2$ ,  $\sigma_a^2$ , and  $\sigma_f^2$  are the variances of observation errors, apparent errors, and model forecast errors, respectively.

In this study, we calculate the statistics of observation errors for a one month period using both local and nonlocal operators. The GPS RO soundings from 15 August to 15 September 2003 from CHAMP (CHALLENGING Minisatellite Payload) and from 15 July to 15 August 2006 from FORMOSAT-3/COSMIC were used for the errors in statistics, respectively. The amounts of the GPS RO in the simulated outermost domain (with 151 by 151 grids at horizontal resolution of 45 km) vary with height for both data sources (Fig. 1a). The number of GPS RO from FORMOSAT-3/COSMIC is about two to three times more than that from CHAMP at lower levels and about 1.7 times above 8 km (where the amounts are 314 for CHAMP and 546 for FORMOSAT-3/COSMIC). Evidently, there are only small differences between the statistics of the observation errors at all vertical heights for the two data sources (Fig. 1b), except below 6 km where a larger difference arises possibly due to the data scarcity for CHAMP at lower altitudes. The observation error produced by local operator shows an approximately exponential decay with a maximum in the lowest level of about 3%, which is consistent with the estimate of Chen et al. (2006) using a 50-km resolution. The nonlocal operator produces smaller errors even at the lowest height, and the errors are generally less than 1% at all the levels and 0.5% above 6 km. Hence, the observation errors produced by the nonlocal operator are about two times smaller than those by the local operator, which is in good agreement with Sokolovskiy et al. (2005b). With the similar observation errors as estimated from CHAMP and FORMOSAT-3/COSMIC, we adopt the profiles of observation error statistics with a modified curve in the lowest level of 2 km for the nonlocal operator. Due to less confident statistics from fewer GPS RO points at lower levels for the CHAMP data, we have leveled off the observation errors below 2 km as supported by the FORMOSAT-3/COSMIC data.

### 3. EXPERIMENTS AND MODEL RESULTS

#### 3.1 Model Setting and Experiment Design

To assess the potential impact of the FORMOSAT-3/COSMIC data on model simulation, we simulate a typhoon event to demonstrate the performance of the nonlocal operator. Several typhoons occurred in the northwest Pacific be-

fore August 2006 in the earlier adjustment stage of the six satellites after launch. One of the typhoons, Kaemi, is particularly interesting since it made landfall in southeast Taiwan and brought torrential rainfall during its passage. To simulate Typhoon Kaemi, we use WRF model with three nested domains at horizontal resolutions of 45, 15, and 5 km, respectively (Fig. 2). According to the analysis by CWB (the Central Weather Bureau) in Taiwan, Typhoon Kaemi possessed a moderate intensity with a maximum wind speed of  $38 \text{ m s}^{-1}$  when it, born southwest of Guan on 19 July, intensified to a moderate typhoon on 21 July. Kaemi persistently headed west-northwestward for Taiwan and made landfall at Tai-Tung (the southeast county of Taiwan) at 1545 UTC 24 July. At 0000 UTC 25 July, the typhoon center had left Taiwan, but the outer circulation still surrounded the whole island. The near-surface wind from NCEP AVN (global model) analysis at 0000 UTC 23 July 2006 (the initial simulation time) is shown in Fig. 2. The central low pressure of 997 hPa for Kaemi is considerably weaker than the obser-

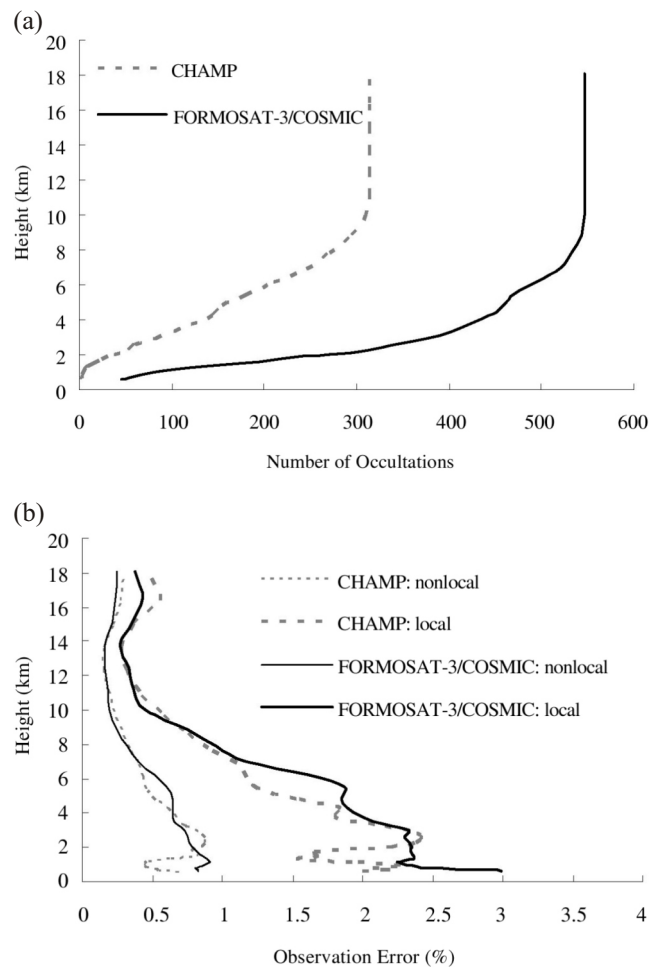


Fig. 1. (a) The amounts of GPS RO varied with height. (b) The statistical observation errors for local (right) and nonlocal (left) operators with CHAMP data (2003/08/15 - 2003/09/15) and FORMOSAT-3/COSMIC data (2006/07/15 - 2006/08/15).

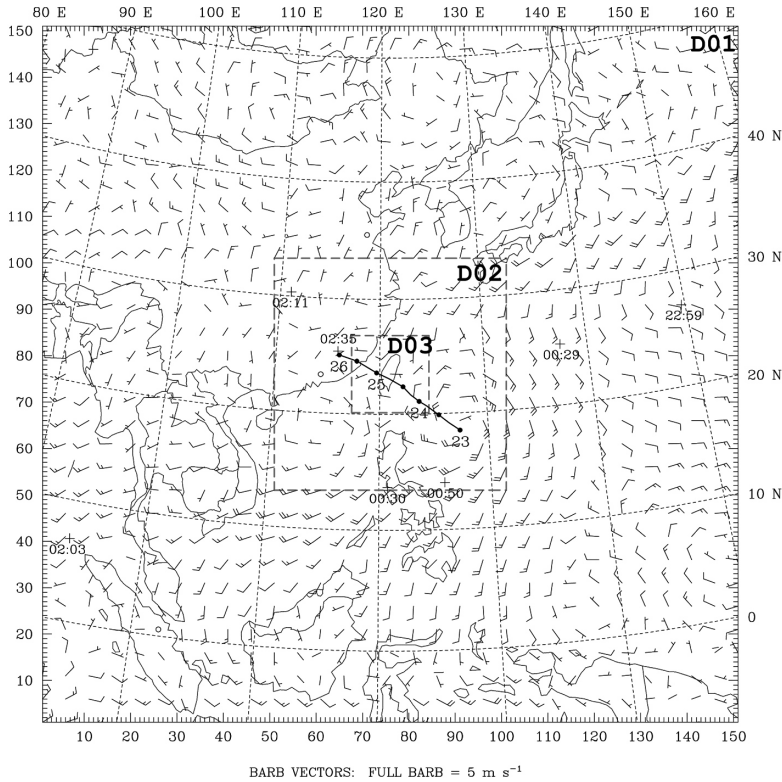


Fig. 2. The near-surface wind from a NCEP AVN analysis in the outermost domain at the initial time, and the best track (indicated by the date) from the CWB for Typhoon Kaemi (2006). The model simulation domains with horizontal resolution of 45, 15, and 5 km, respectively, are depicted. The plus signs indicate the occultation positions available for assimilation and their corresponding UTC times.

vation (960 hPa) at this time (figures not shown).

The model simulations employ the cumulus parameterization of the Kain-Fritsch scheme in two outer domains and the cloud microphysics scheme of Lin et al. in all the domains. The first guess for WRF 3DVAR was taken from the NCEP AVN analysis which also provided the boundary condition for the outermost domain. The model was initialized at 0000 UTC 23 July, within

3 h of which seven GPS RO events took place in the outermost domain. The data assimilations were performed in all of these three domains. Seven soundings with occultation times are marked by a plus sign in Fig. 2. One observation location (occurring at 0050 UTC) nearest to the typhoon center was about 600 km away. We conducted the simulations without assimilation of GPS RO data (denoted by NONE) and with assimilation of refractivity using the nonlocal operator and the so-called local operator variant (denoted by EPH and LLZ, respectively) for comparisons, see Table 1. The main reason for introducing LLZ is that it allows an accounting for the horizontal smears of tangent points as EPH and testing

Table 1. Summary of numerical experiments.

<b>initial time: 0000 UTC 23 July 2006 (integrated for 72 h)</b>	
<b>Experiments</b>	<b>Description</b>
NONE	No assimilation
LOC	Assimilated with GPS refractivity by using a local operator
LLZ	Assimilated with GPS refractivity by using a local operator variant
EPH	Assimilated with GPS refractivity by using a nonlocal operator
GTS	Assimilated with GTS data and QuikSCAT data
GTS+EPH	Assimilated with GTS data, QuikSCAT and GPS data
EPH+TCBOG	Assimilated with GPS data and a bogus vortex for the typhoon using a nonlocal operator
GTS+EPH+TCBOG	Assimilated with GTS data, GPS data and the bogus typhoon
<b>Sensitivity Experiments</b>	
EPH_RE2A (time: 0030, 0050)	The same as experiment EPH, but two GPS RO points [(13.717°N, 120.752°E) and (14.095°N, 125.859°E)] were removed, which are close to the typhoon center at the initial time
EPH_RE2B (time: 0211, 0235)	The same as experiment EPH, but two GPS RO points [(30.432°N, 111.060°E) and (25.504°N, 115.948°E)] over east China were removed
LLZ_2ER	The same as experiment LLZ except using double observation errors
EPH_2ER	The same as experiment EPH except using double observation errors

the effect of different observation errors. Modifying the default local operator built into the WRF 3DVAR for testing these effects requires more technical work. For both EPH and LLZ, the cost function is calculated on the model mean heights (about 31 levels) using same interpolation schemes. A simulation with refractivity assimilation on the observation heights was also conducted for the default local operator in WRF 3DVAR (denoted by LOC) but with smoother observation errors based on the statistics in Fig. 1b (Ma et al. 2006). Note that the cost function is calculated on all observation heights (normally consisting of about 200 levels) for LOC.

Typhoon predictions are intimately influenced by how the initial typhoon vortex is resolved by the model. Some vortex bogussing in 3DVAR might be useful for improvement of model performance. On the other hand, bogus data assimilation (BDA) (e.g., Zou and Xiao 2000) using the dynamic model in 4DVAR has been proposed and shown to be robust for initialization of an intense vortex with asymmetric structures. In this study, a symmetric balanced vortex as routinely adopted by CWB is used to represent a bogus typhoon to be assimilated in 3DVAR. We denote the relevant experiments with a bogus vortex by attaching a name “TCBOG”. Similarly, a name “GTS” is also attached in relevant experiments with conventional soundings in view of the availability of these routine data. In this study, the QuikSCAT wind field during the assimilation time window is also combined with the conventional data.

For identifying the influence of individual GPS RO soundings, two additional experiments (EPH\_RE2A and EPH\_RE2B) were conducted in which two GPS RO points closest to the typhoon vortex or over China near the initial time are removed, respectively. Sensitivity tests on the statistic observation errors were also conducted to justify the gross model performance with the default errors. All of the experiments were integrated over 72 hours. During the model integration, the prediction in the finer domain with lateral boundary conditions specified from the prediction in the outer domain is used to update the latter prediction on their overlapped points as “an interaction of two ways”.

### 3.2 Increment Analyses

Ingestion of the seven GPS RO refractivity soundings produces sizable initial increments, i.e., the differences between the initial fields with and without GPS RO assimilations, as shown in Fig. 3 for the analysis level at 806 hPa where the increments are found to be relatively larger. The panels, from left to right denote the increments of temperature, water vapor mixing ratio and refractivity, respectively, for experiments EPH, LLZ, and LOC (from the top to bottom panels, respectively). In general, the increments of temperature (Figs. 3a, d, g), moisture (Figs. 3b, e, h) and

refractivity (Figs. 3c, f, i) produced by the three different operators have similar geometric distributions. Also, the increments for these operators appear to have same signs for most of the impact regions. However, some of them are in opposition. For example, the temperature increments are positive for EPH and LLZ at RO point 1 which is indicated in Fig. 3a, while they are negative for LOC. The moisture increments south of Japan (RO point 2) are positive for EPH and LLZ, while they are negative for LOC. Contributions from RO point 4 are negative for EPH, while they are very weakly positive for LLZ and almost near zero for LOC. The increments for refractivity and moisture exhibit similar distributions since the largest contribution of refractivity variations comes from the moisture term in (1). We note that the shapes of the moisture and refractivity increments for EPH are more elliptical as compared to those for LLZ and LOC. The long axis of the elliptic contour is primarily along the direction of ray propagation, reflecting the effect of ray integration from the perigee point, especially for RO point 2. For LLZ and LOC, the increments are more symmetric with respect to the perigee point, resulting from assimilation of local refractivity. The responses of the assimilation to wind increments are generally weak, as a typical result of the associated small temperature changes with a hydrostatic balance in 3DVAR (Huang et al. 2005).

At a higher level, 433 hPa, most of the increments also preserve the same sign (Fig. 4), except for the moisture increments in east China (RO point 7) that are positive for LLZ and LOC but are negative for EPH. The horizontal scope of the increments is similar to that at lower levels for each operator (see Fig. 5 for some cross sections). Magnitudes of the increments produced by the three operators are also quite similar and are closer at 433 hPa than at lower levels. As expected, the different behaviors of the operators are more prominent at lower levels where atmospheric refractivity is much larger and less homogeneous. This is because the spherical symmetry approximation becomes less valid and the use of a nonlocal operator is more appropriate to reduce the error of the forward model. Again, the increments at 433 hPa produced by the nonlocal operator (EPH) exhibit elliptic shapes elongated along the ray compared to rather circular contours produced by the local operator variant (LLZ) and the local operator (LOC).

For a clearer picture of vertical variations, increments in the vertical cross-section along the ray paths of three selected RO points (points 2, 4, and 7, marked in Fig. 4a) are inspected. Herein, we show in Fig. 5 the relative change of refractivity after the assimilation at the cross sections along the three RO ray paths which are nearer to the typhoon center. The vertical distributions of the extreme high and low values produced by these three operators are mainly in phase, although differing in some details. In general, the increments are graded more clearly for LLZ (Figs. 5d, e, f) and LOC (Figs. 5g, h, i) than EPH (Figs. 5a, b, c). The ray inte-

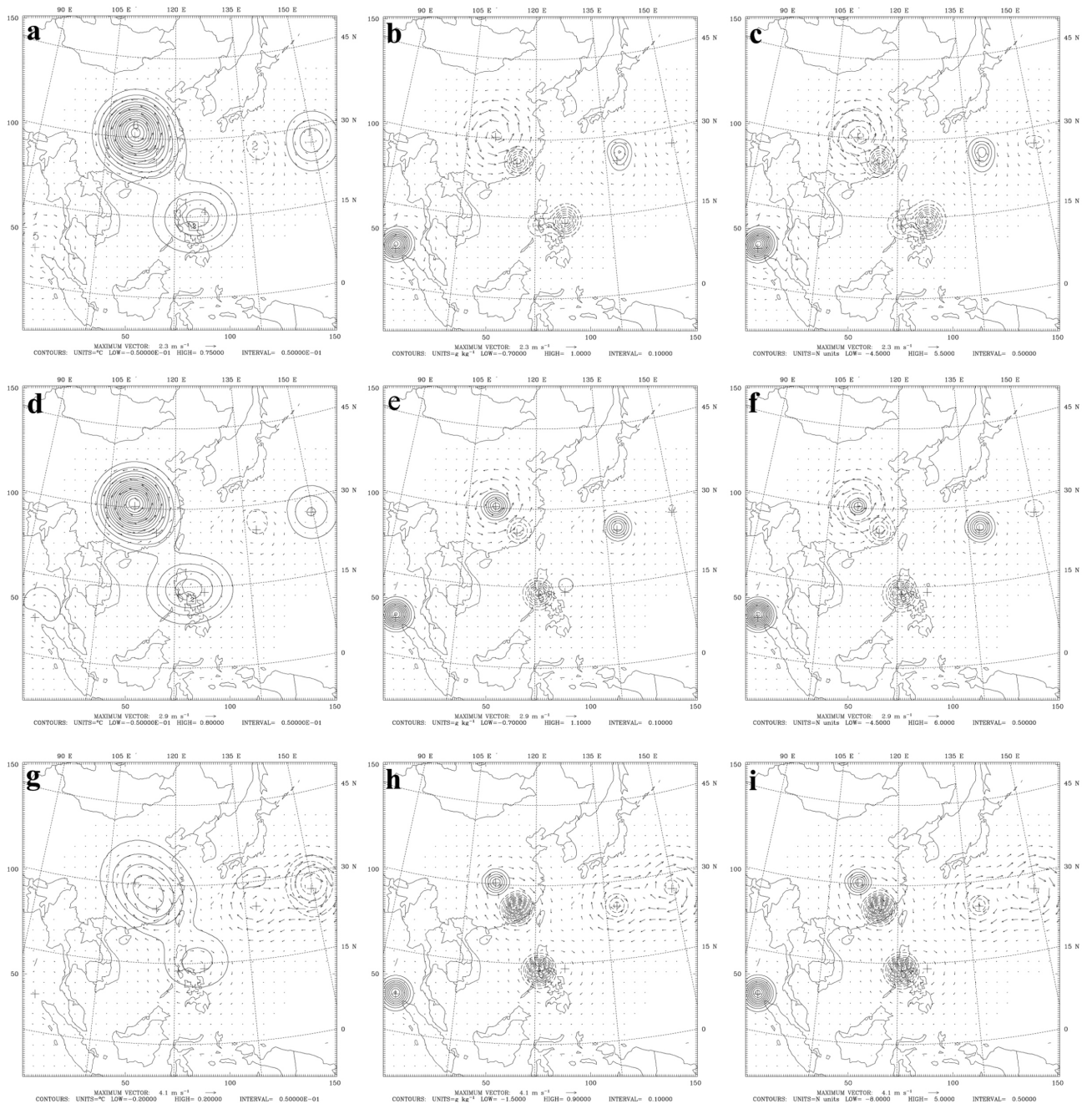


Fig. 3. Initial increments for (a) temperature (at an interval of 0.05 °C), (b) water vapor mixing ratio (at an interval of 0.1  $\text{g kg}^{-1}$ ), and (c) refractivity (at an interval of 0.5 N-units) at 806 hPa produced by the nonlocal operator. The increments for horizontal wind at the same level are also overlapped. Panels (d), (e), and (f) as in (a), (b), and (c), respectively, but for the local operator variant, and (g), (h), and (i) for the local operator. The plus signs indicate the occultation positions. The numbers in (a) indicate the RO points.

gration appears to smooth out the vertical influence of local refractivity in the vertical column. As a result, vertical variations are sharper with greater maxima for both LLZ and LOC. Overall, the maximum refractivity increments are less than 4% for the three operators. The position of the center at a maximum or minimum slightly tilts with height for EPH and LLZ as compared to that for LOC because the locations of the tangent points change slightly with height for the for-

mer two. The observations are assimilated on the observation levels for LOC, but on the model mean heights for both EPH and LLZ. That is the reason why more similar representations occur by EPH and LLZ than that by LOC at higher levels. At lower heights, the vertical model resolution is higher than that at higher levels. Thus, the features exhibited by LLZ are more similar to those by LOC at lower heights indicating that the ray integration for EPH produces con-

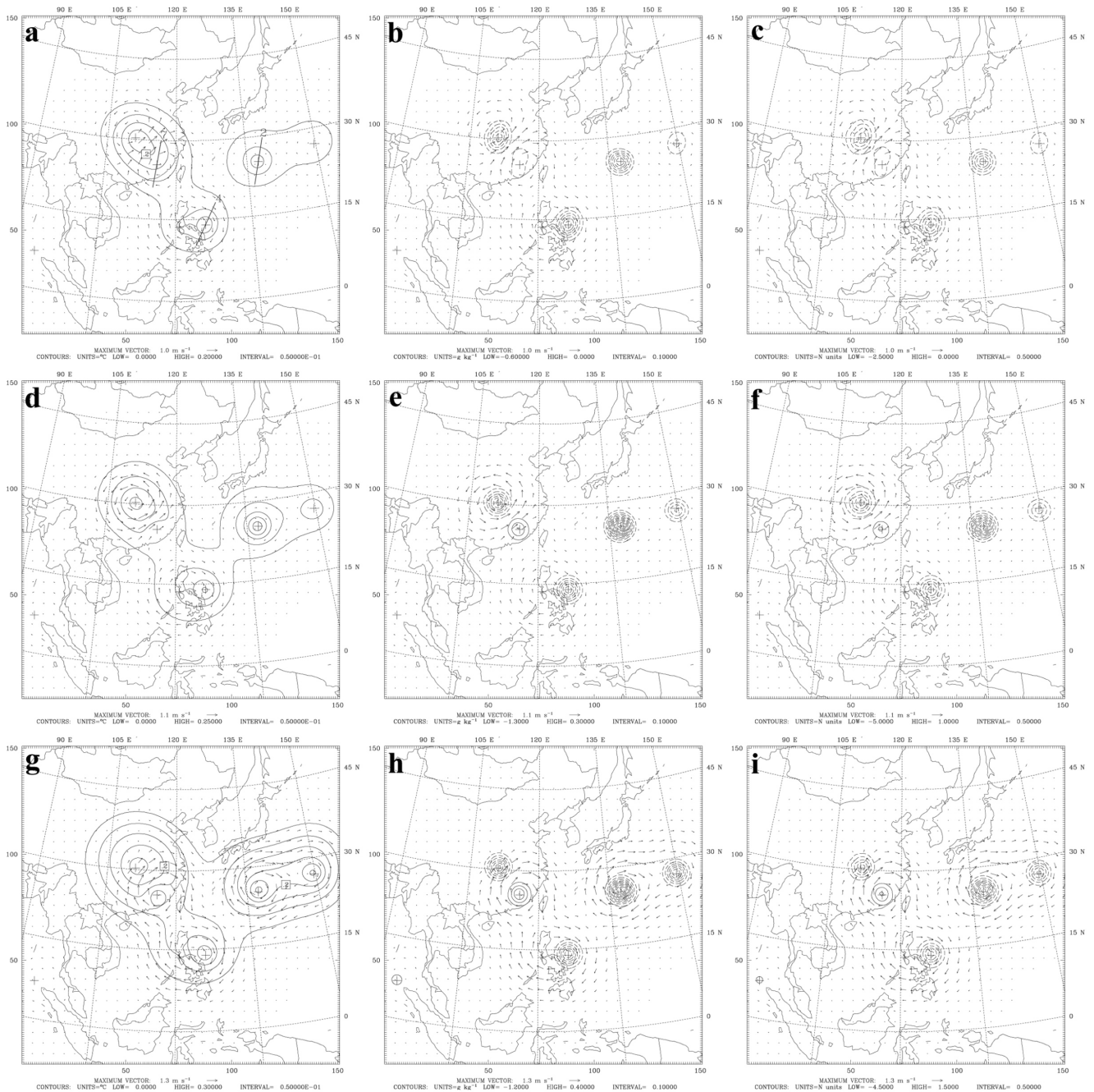


Fig. 4. The same as in Fig. 3 but at 433 hPa.

siderable influence on the minimization.

The fractional differences in excess phases between the analysis (A), background (B), and the observation (O) are examined for several occultations, as shown in Fig. 6. The fractional differences of O-B for EPH are less than 1% even at lower levels, which is consistent with Sokolovskiy et al. (2005a, b). Based on the analyses, most of the profiles exhibit a negative bias at lower levels for EPH (Fig. 6), LLZ, and LOC (figures not shown) as presented by Rocken et al. (1997). The standard deviations (SD) of

the above introduced fractional differences for seven GPS RO soundings are shown in Fig. 6e for EPH and in Fig. 6f for LLZ. The differences of SD for EPH are always less than that for LLZ; the latter differences are about two to three times larger than the former. This indicates that the ray integration for EPH does result in a reduction of the representativeness error by LLZ. After assimilation, both the adjusted excess phase and refractivity are closer to the observations, i.e., with magnitudes of O-A are more reduced than those of A-B.

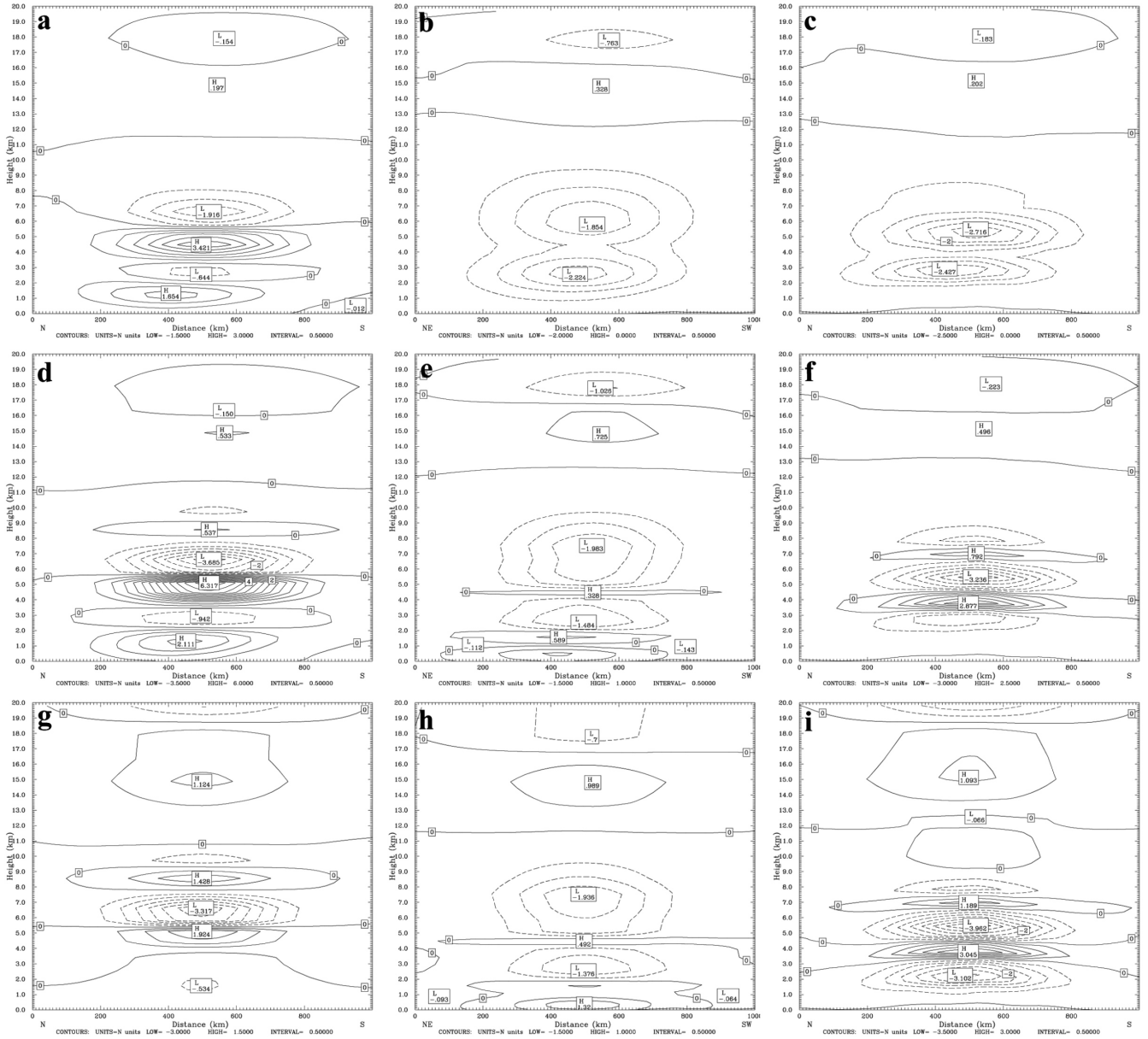


Fig. 5. The initial fractional increments of refractivity (the differences between the analyses with and without assimilation) at the vertical cross sections along the ray through RO points (a) 2 at (25.347 , 137.421 ), (b) 4 at (14.095 , 125.859 ), and (c) 7 at (25.504 , 115.948 ) at an interval of 0.5% for the nonlocal operator. Panels (d), (e), and (f) as in (a), (b), and (c), respectively, but for the local operator variant, and (g), (h), and (i) for the local operator.

### 3.3 General Performance

The analysis field after assimilation was then used for a 72-h model integration. The simulated typhoon tracks (based on the position of minimum sea-level pressure) are shown in Fig. 7 for the four experiments, NONE, LOC, LLZ, and EPH. Without relocation for the typhoon center at the initial time, the initial vortex in the model as resolved by the NCEP AVN data differs slightly from the observed location. Consequently, early in the simulation the simulated tracks for the four experiments are slightly northward as compared to

the CWB best track. The simulated typhoon centers generally move west-northwestward toward Taiwan and then make landfall in southeast Taiwan for NONE, EPH, and LLZ; there is no landfall for LOC. However, their landfall times are considerably delayed by about 6 - 12 h compared to the actual time (39 h). Prior to 24 h, most of the simulated typhoon tracks are similar, all to the north of the best track. After 24 h, the simulated typhoon centers for the three landfall cases have moved to the south of the best track. Although most the simulated typhoons make close landfall positions near the southern tip of Taiwan, the landfall posi-

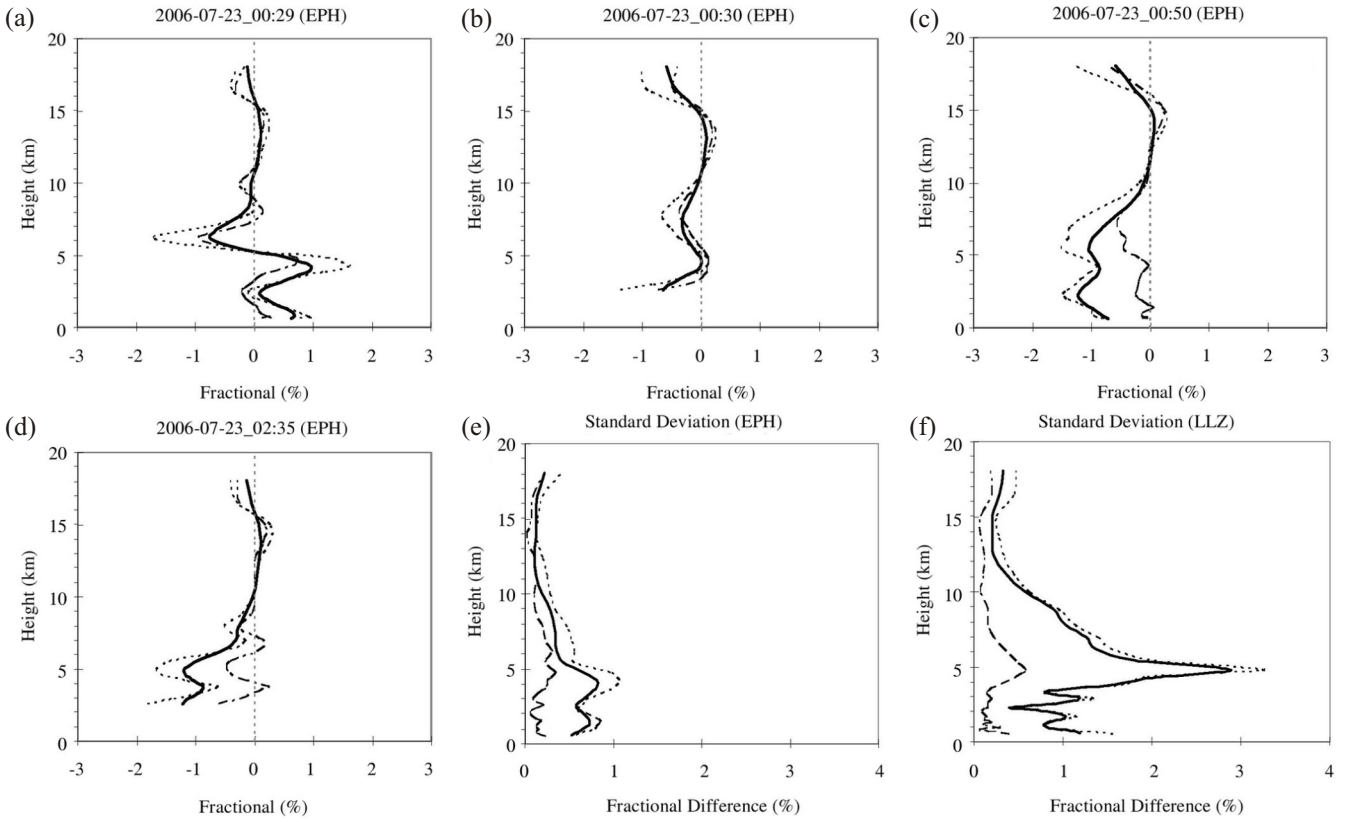


Fig. 6. The fractional differences of excess phase (S) for  $(S_A - S_B) / S_O$  (solid line),  $(S_O - S_B) / S_O$  (dotted line), and  $(S_O - S_A) / S_O$  (dashed line) by the nonlocal operator for the RO points (a) 2, (b) 3, (c) 4, and (d) 7. Panel (e) as in (a), but for fractional standard deviation of seven GPS RO points for the nonlocal operator and (f) the local operator variant. Here, A, B, and O represent the analysis, background and observation fields, respectively.

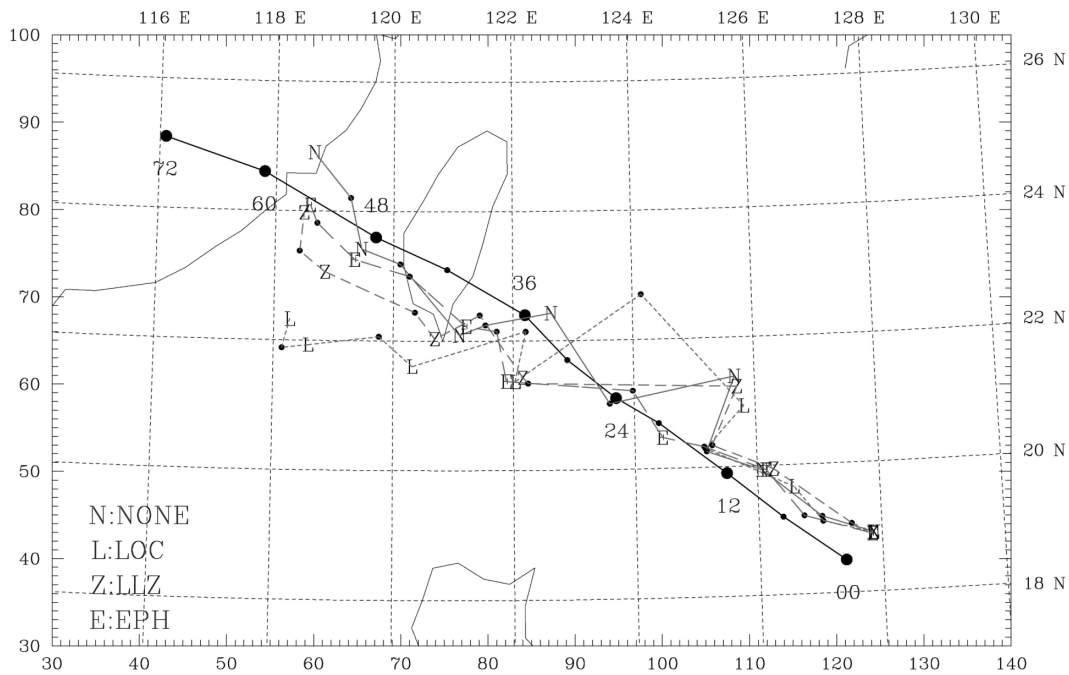


Fig. 7. The best track from the CWB (denoted by bold-solid circles) at 12-h intervals accompanied with the integrated hours. The simulated tracks for experiment NONE are denoted by "N" (gray-solid line), LOC by "L" (dotted line), LLZ by "Z" (dashed line), and EPH by "E" (longer-dashed line).

tion for EPH is closest to the observed than the others. After passing over Taiwan, the simulated typhoons with a landfall tend to move northwestward in concert with the observed direction by the end of the simulation time.

For a statistical evaluation for the four experiments, the mean track errors in every 24 hours are inspected and are depicted in Fig. 8. For the first day, EPH gives the smallest track error of about 80 km and greatly outperforms the other three experiments. However, this outperformance somewhat degrades with time for the second and third days. Without vortex bogussing, the initial typhoon central pressures are about 997 hPa for the four experiments and are much weaker than the observed value, 960 hPa from CWB or 955 hPa from JTWC (Joint Typhoon Warning Center) (Fig. 8b). Even in the assimilation experiments with a bogus vortex for EPH+TCBOG and GTS+EPH+TCBOG (Table 1), their typhoon central pressures are only about 989 hPa (figures not shown). The GPS RO data from the three assimilation experiments appear to have less impact on typhoon intensity forecasting producing similar variations of the intensity with time as those for the no-assimilation experiment (cross sign). The typhoon intensity for NONE is stronger after 24 h than that in the three assimilation experiments, but less consistent with observations after 48 h. With landfall positions further south of the island than the observed, the typhoons for the assimilation experiments still slightly intensify with time while the real typhoon quickly weakened after making landfall. For this typhoon case, there are no significant forecast differences in typhoon intensity when assimilating the same GPS RO data with different operators.

### 3.4 Local Circulation near Taiwan

In the previous section, the overall performances for the experiments using different operators were shown with a fo-

cus on typhoon tracking and intensity forecasting. It is interesting to look into further details of the impact on the simulated local circulation near Taiwan that might produce prominent differences in verifiable rainfall over the island. The sea-level pressures and near-surface wind field in the innermost domain are shown in Fig. 9. As mentioned before, the typhoon vortex center has intensified to 971 hPa at 48 h (Fig. 9b) and to 969 hPa at 60 h (Fig. 9c). For the three assimilation experiments, their vortex cores (Figs. 9d, e, f) are less organized compared to that without assimilation. Evidently, assimilating the GPS RO data has produced significant effects on the typhoon development. The local circulations at 48 h with a vortex core just off southeast Taiwan coast are much more similar for EPH (Fig. 9f) and LLZ (Fig. 9e) than that for EPH and LOC (Fig. 9d). Indeed, LOC has produced a more southward biased track at this time, with a vortex core to the south of Taiwan.

### 3.5 Simulated Rainfall over Taiwan

Since we have observed more moisture modifications (increments) at lower levels from the assimilation of GPS RO soundings, it is interesting to see whether rainfall prediction will be influenced, given similar track predictions for the assimilation experiments. The observed rainfall distributions are quite different at various stages of a typhoon which approached or passed Taiwan. In the first day (0000 UTC 23 - 24), rainfall was sparse except for a local event over southwest Taiwan which was not related to the typhoon circulation (not shown). Kaemi then brought most of the rainfall over the eastern portion of the island over the second day (0000 UTC 24 - 25) with a maximum of 348 mm over the southern slope of the Central Mountain Range (CMR) in Taiwan (Fig. 10a). In the third day (0000 UTC 25 - 26), the rainfall in general significantly weakened except

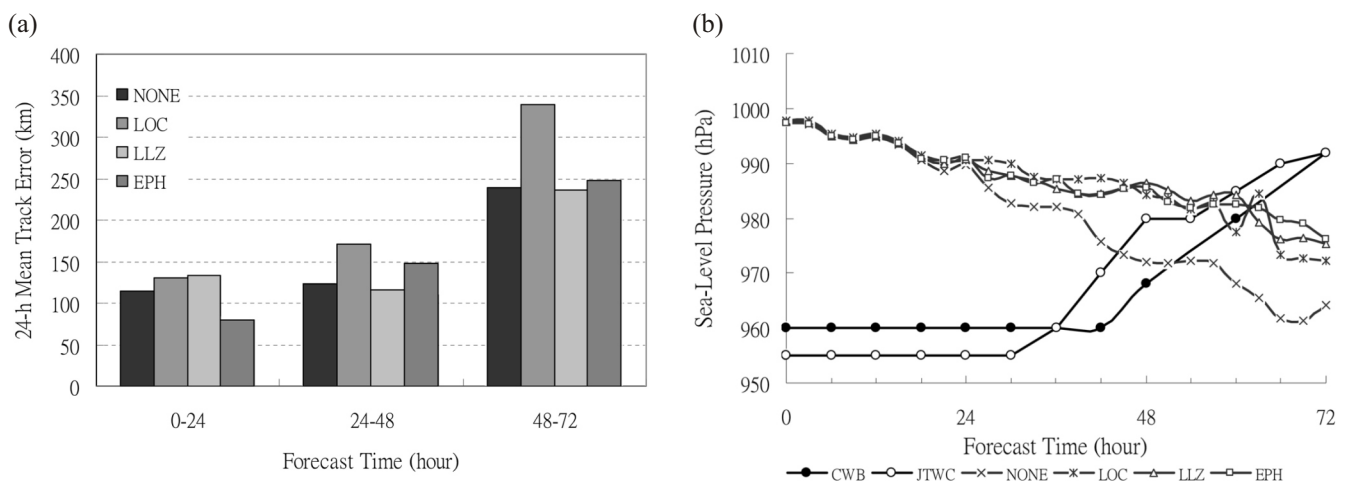


Fig. 8. (a) The 24-h mean track errors (unit: km) for experiments NONE, LOC, LLZ, and EPH, and (b) the sea-level pressure (unit: hPa) at typhoon centers varied with time from CWB (solid circle), JTWC (open circle), and the four simulations.

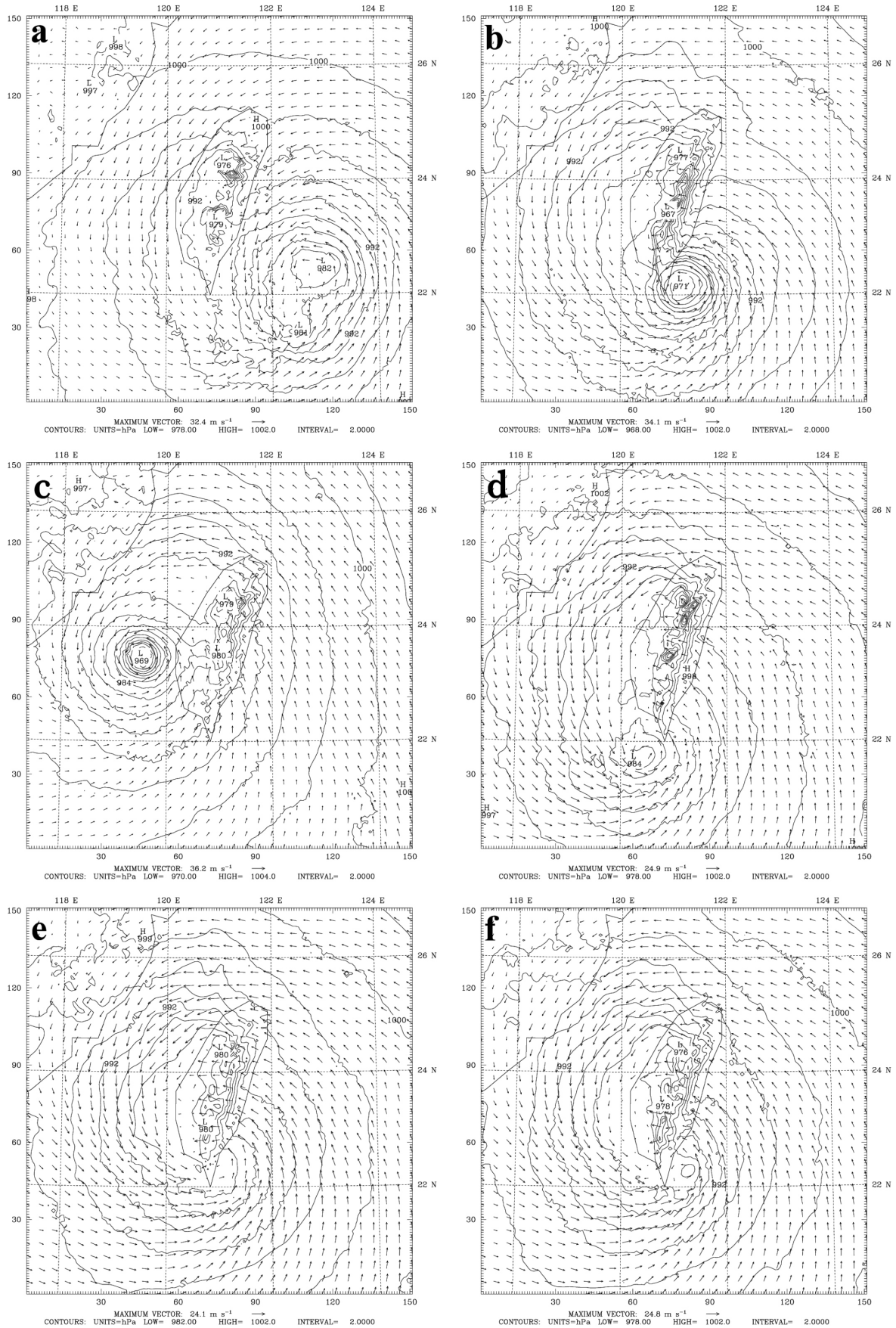


Fig. 9. The simulated sea-level-pressure (unit: hPa) and near-surface wind (unit: m s<sup>-1</sup>) for experiment NONE at (a) 36, (b) 48, and (c) 60 h; (d), (e), and (f) as in panel (b) but for experiments LOC, LLZ, and EPH, respectively.

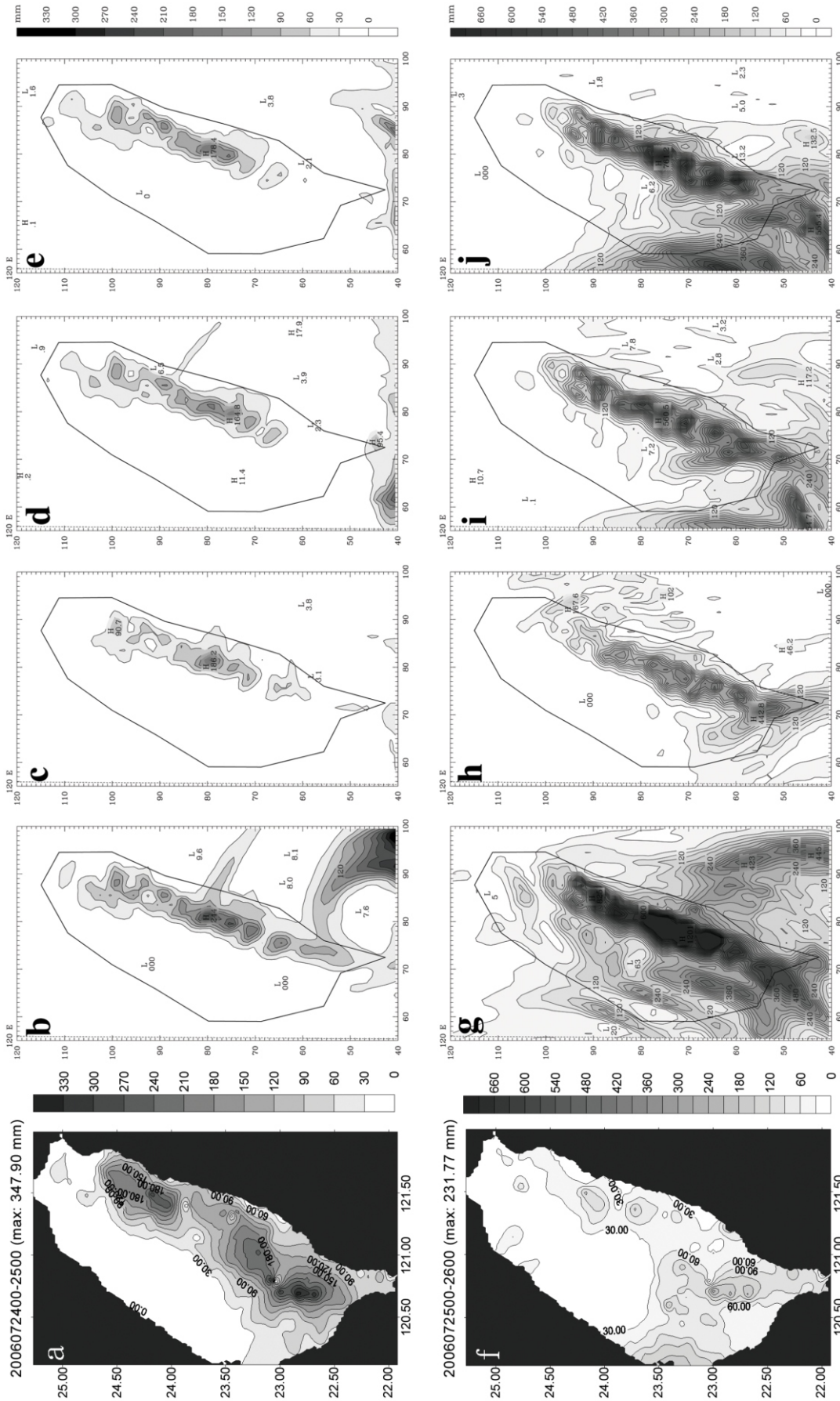


Fig. 10. The simulated 24-h accumulated rainfall with an interval of 30 mm for the second day (0000 - 2400 UTC 24 July 2006) for the experiments (b) NONE, (c) LOC, (d) LLZ, and (e) EPH. (f), (g), (h), (i), and (j) as in (a), (b), (c), (d), and (e), respectively, but for the third day (0000 - 2400 UTC 25 July 2006). (a) and (f) are the corresponding daily rainfall observations in the second and third days, respectively.

for the southwest plain of Taiwan (Fig. 10f). The intense rainfall in east Taiwan was related to the impinging upslope flow in the northwestern flank of the typhoon circulation. In addition to the observations, Fig. 10 also shows the simulated 24-h accumulated rainfall for the experiments NONE, LOC, LLZ, and EPH for the second and third days. Thus, when the simulated typhoon vortex approaches Taiwan, most of the simulated precipitation is produced over east Taiwan as observed (Figs. 10b, c, d, e). In the second day, observations show a rainfall maximum (between 22.5 N and 23 N) over the southern CMR, which is not well captured by any of the experiments (NONE, LOC, LLZ, and EPH). Only the experiment NONE produces considerable rainfall further South due to the effect of a more intense flow associated with the stronger vortex core (Fig. 9b). For the other three experiments, the simulated rainfall patterns are generally similar.

In the third day, all of the four simulations show severe overprediction of rainfall on the eastern island (Figs. 10g, h, i, j), especially for NONE giving a maximum accumulated daily rainfall over 1200 mm. Indeed, the rainfall for NONE has also exhibited overall overprediction on the entire island. This overprediction, however, is somewhat abated in the three assimilation experiments. Among the three assimilation experiments (Figs. 10h, i, j), it appears that the observed rainfall maximums on the southwestern and southern island are better captured by EPH. To examine the contributions of GPS RO soundings to the local rainfall prediction, we conducted sensitivity tests by removing several GPS RO soundings. When two GPS RO soundings over east China were discarded in the experiment EPH\_RE2B (Table 1), the rainfall distributions (figures not shown) for the three days were similar to those for EPH. The other sensitivity test which removes two GPS RO soundings near the Philippines (experiment EPH\_RE2A) shows similar rainfall as those for EPH in the second day, but gives a much larger maximum (888 mm) over southern Taiwan in the third day (not shown).

#### 4. SENSITIVITY TESTS AND DISCUSSIONS

The previous section presented simulated results compared with some observations for several experiments using different observation operators. Their simulation results indicated that assimilation of GPS refractivity data by a local operator and nonlocal operator may have some impact on model performance solely due to the modification in initial analysis. However, these impacts should be evaluated in a more objective manner. In addition, it is also essential to explore other combined effects such as the inclusion of a bogus vortex, cycling experimentation and assimilation of conventional GTS soundings, all of which are now implemented in routine operations. Some experiments were designed in this study to address these issues in order to ex-

plore whether more impacts will be produced. Hence, we will mainly focus on further examination of the performances for all the experiments on verifiable rainfall prediction over the island. The impact of GPS RO data assimilation using the new operator will also be analyzed.

#### 4.1 Sensitivity Tests

For routine operations for typhoon prediction, the CWB has implemented a bogus vortex from a solution of balanced Rankine vortex at six mandatory vertical levels. This bogus vortex (with an estimated intensity of 965 hPa) is then assimilated as “observations” into the model initial condition for the three domains. Figure 11 shows the simulated sea-level pressure and near-surface wind in the outermost domain at the initial time for EPH+TCBOG. There are total of 40 bogus observations for the typhoon vortex (dot points as indicated in Fig. 11). The analysis after assimilation for typhoon has a stronger intensity of the central low pressure (989 hPa) than that (only about 997 hPa) in the other experiments without vortex bogussing.

Figure 12 shows the typhoon track predictions for the experiments with the bogus vortex and other sensitivity tests as described before. From homogeneous comparisons (GTS and GTS+EPH), their tracks are very close, indicative of the reduced impact when GTS soundings are also assimilated. The inclusion of an initial bogus vortex in the experiments (EPH+TCBOG and GTS+EPH+TCBOG) has degraded the performance without vortex bogussing. This may be due to the fact that the bogus vortex after relocation was not strong enough to reproduce the intensity of the observed typhoon. Thus, there will be a more complicated issue involving both cycling and bogussing, and such an exploration is currently not within our scope targeting on the impact of the GPS data assimilation using the developed operators.

#### 4.2 Evaluation of Model Performances

The above tests and comparisons have presented a broad spectrum of model performance; however, definite conclusions may not be easily made and may be partly due to the fact that not so many GPS RO soundings have been assimilated within the experiments and also because typhoon prediction usually encounters more intricate problems. Further, different biases from observation assimilations may interact with each other demanding a much more detailed evaluation. Figure 13 depicts the daily average track errors (in km) over the three days for each of the experiments in this study. Overall performances of different runs are comparable. Indeed, the first daily track error for EPH is the best (around 80 km) among each of the experiments, and the performance still ranks high in the second day but slightly degrades by the third day. On average, LOC gives worse performances in the second and third days compared to LLZ and EPH. The

combined assimilation of both GPS and GTS soundings doesn't always outperform the assimilation with GPS data only. Doubling the covariance error for the observation operator has shown some variations in performance but not as much as in the runs with vortex bogging. Removal of some RO soundings (EPH\_RE2A and EPH\_RE2B) gives somewhat similar performances as those for EPH, but the latter (EPH\_RE2B) seems to give a larger impact on average. Further analysis on the processes producing an impact will be given later.

For an objective evaluation on verifiable rainfall, the threat score (TS) and root-mean-square error (RMSE) are calculated for the daily accumulated rainfall over Taiwan in the second and third days for each of the experiments in this study. The TS as verified against observations (see Huang et al. 2005) with the thresholds of 0.25, 0.5, 1, 2, 5, 10, 15, 20,

25, 50, and 100 mm and RMSE are listed in Table 2. Maximum daily rainfall amounts depicted by grid overlays covering the island are also presented for the observations and different simulations in Table 2. For each of the experiments, the TSs for both days are higher than 0.5 for smaller thresholds (less than 5 mm) but decrease sharply with increasing thresholds. For the second day, there is no advantage of the assimilation experiments over the unassimilated experiments. The performances for smaller thresholds are improved by inclusion of GTS soundings but become worse than NONE for larger values (e.g., 5 mm and higher). The combination of both GTS and GPS data (e.g., GTS+EPH) also has no significant impact for all thresholds as compared to the experiment with GTS only. Inclusion of a bogus vortex (EPH+TCBOG) resulted in a degradation of TS for smaller thresholds but helped improve the scores for higher

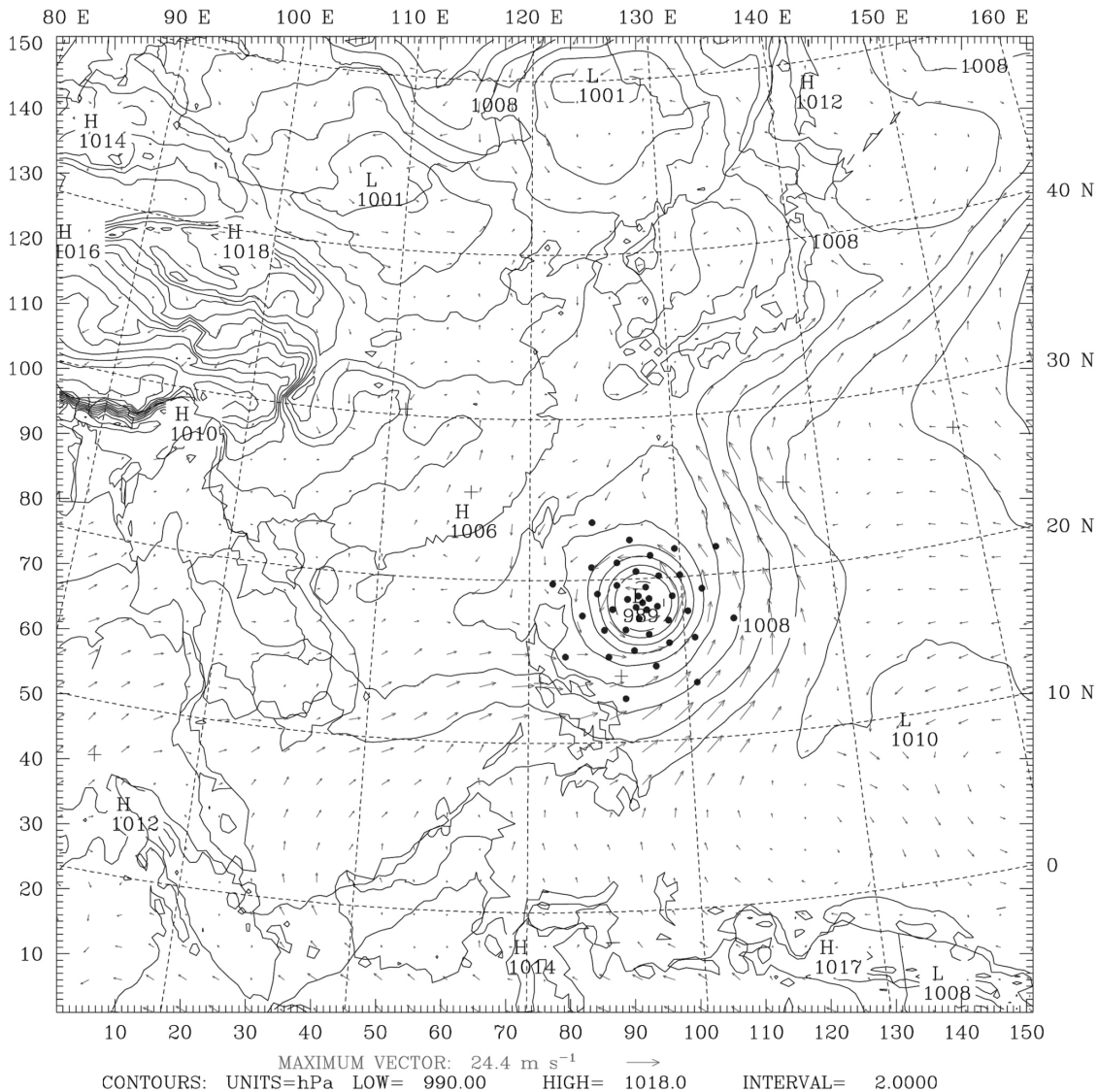


Fig. 11. The sea-level-pressure (unit: hPa) and near-surface wind (unit: m s<sup>-1</sup>) at the initial time for the experiment EPH+TCBOG. The locations of the bogus typhoon and GPS RO data are indicated by gray circles and plus signs, respectively.

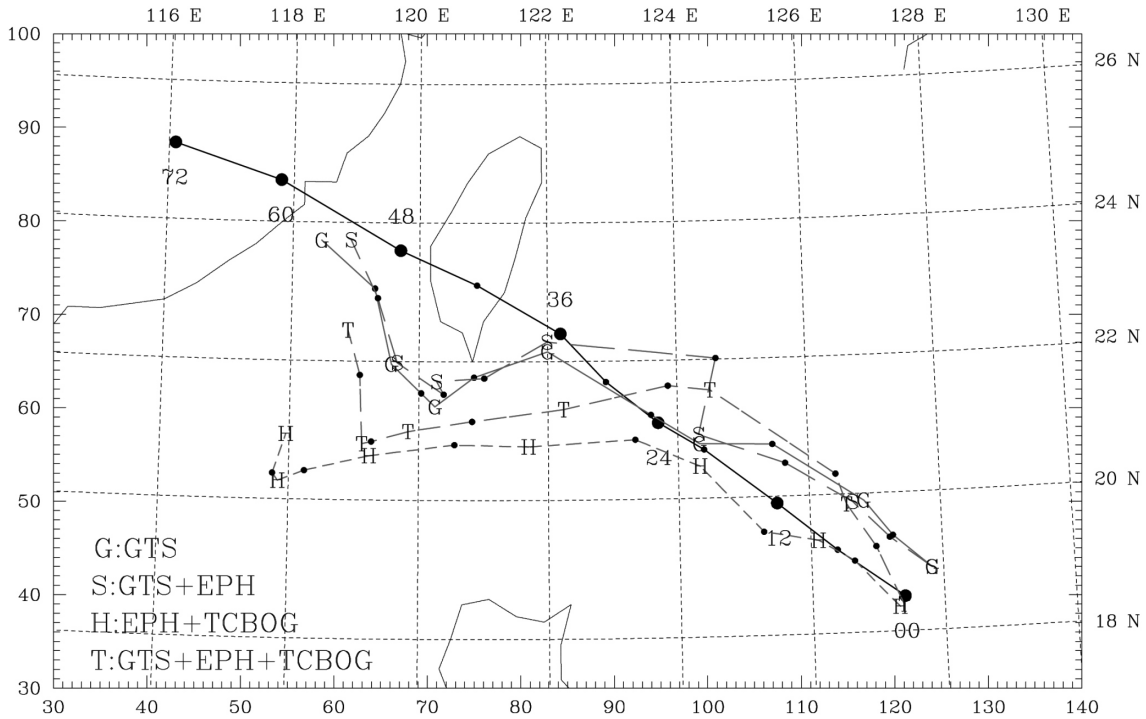


Fig. 12. As in Fig. 7 but for the simulated tracks for experiment GTS indicated by “G”, GTS+EPH by “S”, EPH+TCBOG by “H”, and GTS+EPH+TCBOG by “T”.

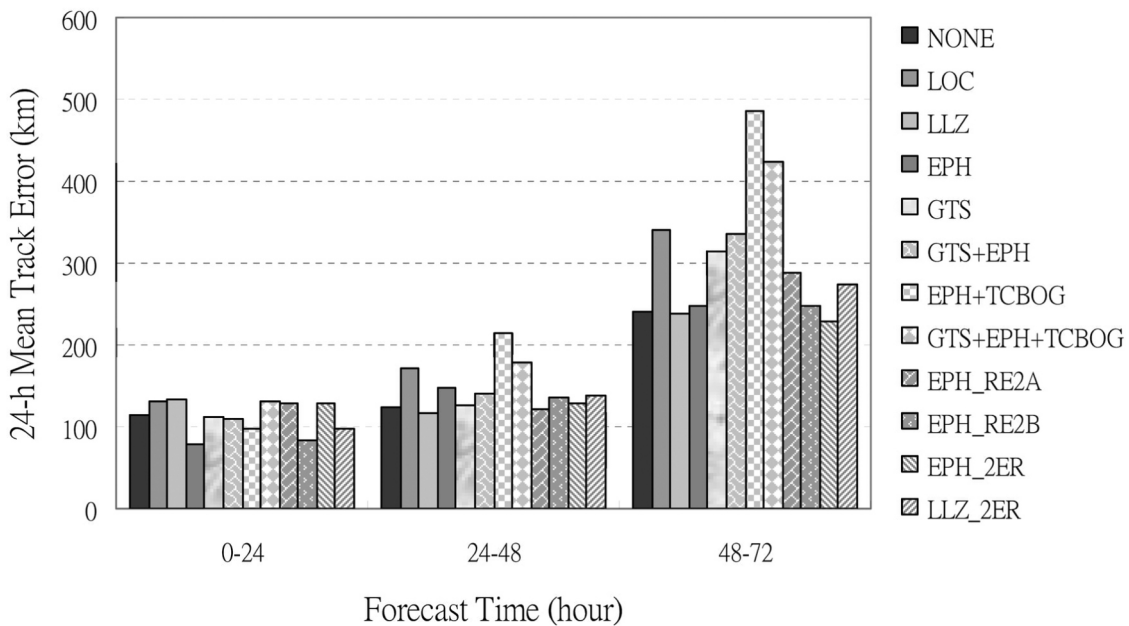


Fig. 13. The same as in Fig. 8a, but for all the experiments.

thresholds as compared to EPH only. This is also true when the GTS data have also been used as shown in (GTS+EPH+TCBOG). Removal of two soundings (EPH\_RE2A and EPH\_RE2B) enhances TS performances for all thresholds and also improves the track prediction. Doubling the

observation covariance errors (LLZ\_2ER and EPH\_2ER) has improved the overall performances for larger thresholds (above 5 mm) for the second day; however, the performances for larger thresholds (above 20 mm) are reversed for the third day.

Table 2. The threat score (TS) and root-mean-square errors (RMSE) (mm) of the simulated accumulated rainfalls between 24 - 48 and 48 - 72 h for different thresholds. The maximum values of the accumulated rainfall observations are 281.2 and 149.9 mm for the second and third days, respectively. The maximum forecast accumulated rainfalls (FCTMX) and 24-h mean track errors (MTE) are also given.

Thresholds (mm)	TS (24 - 48 h)											RMS	FCTMX	MTE
	0.25	0.5	1	2	5	10	15	20	25	50	100			
NONE	0.703	0.655	0.605	0.566	0.552	0.512	0.477	0.452	0.439	0.356	0.146	45.489	244.028	123.426
LOC	0.647	0.625	0.605	0.574	0.511	0.438	0.392	0.353	0.303	0.170	0.024	49.219	186.206	171.600
LLZ	0.718	0.677	0.632	0.576	0.513	0.458	0.401	0.360	0.346	0.234	0.071	48.186	164.765	115.645
EPH	0.680	0.641	0.605	0.568	0.531	0.469	0.398	0.334	0.291	0.193	0.063	49.745	178.381	147.795
GTS	0.809	0.768	0.701	0.625	0.537	0.480	0.426	0.374	0.345	0.243	0.030	47.062	127.835	126.997
GTS+EPH	0.810	0.755	0.691	0.612	0.550	0.475	0.415	0.371	0.345	0.132	0.006	49.345	104.998	140.008
EPH+TCBOG	0.582	0.561	0.534	0.521	0.521	0.470	0.449	0.420	0.376	0.202	0.074	48.052	190.177	213.758
GTS+EPH+TCBOG	0.599	0.582	0.565	0.546	0.551	0.524	0.480	0.445	0.414	0.240	0.083	46.674	160.016	179.017
EPH_RE2A	0.722	0.678	0.638	0.581	0.534	0.476	0.423	0.388	0.365	0.268	0.113	48.236	197.256	121.275
EPH_RE2B	0.749	0.692	0.646	0.600	0.560	0.496	0.444	0.397	0.380	0.274	0.112	47.252	175.805	135.180
LLZ_2ER	0.668	0.629	0.601	0.560	0.541	0.493	0.433	0.391	0.370	0.252	0.084	48.743	181.632	139.180
EPH_2ER	0.665	0.621	0.585	0.545	0.533	0.496	0.447	0.405	0.378	0.259	0.104	47.966	205.875	128.425
Thresholds (mm)	TS (48 - 72 h)											RMS	FCTMX	MTE
	0.25	0.5	1	2	5	10	15	20	25	50	100			
NONE	0.947	0.947	0.946	0.942	0.907	0.836	0.742	0.649	0.596	0.385	0.067	202.239	1200.743	239.540
LOC	0.868	0.838	0.801	0.739	0.674	0.657	0.669	0.680	0.668	0.435	0.086	55.879	442.770	339.438
LLZ	0.934	0.926	0.913	0.885	0.834	0.765	0.729	0.708	0.690	0.490	0.109	79.861	560.476	236.941
EPH	0.947	0.942	0.934	0.922	0.872	0.789	0.731	0.706	0.708	0.547	0.138	113.849	761.219	247.896
GTS	0.928	0.919	0.904	0.880	0.840	0.799	0.744	0.701	0.704	0.532	0.081	98.137	886.956	313.327
GTS+EPH	0.946	0.944	0.932	0.905	0.876	0.828	0.735	0.662	0.647	0.508	0.100	99.401	694.130	335.244
EPH+TCBOG	0.772	0.743	0.687	0.601	0.475	0.370	0.322	0.280	0.228	0.101	0.000	43.327	316.811	485.061
GTS+EPH+TCBOG	0.869	0.853	0.822	0.788	0.706	0.658	0.665	0.705	0.731	0.546	0.086	39.328	446.101	423.397
EPH_RE2A	0.944	0.935	0.927	0.906	0.868	0.802	0.738	0.709	0.712	0.554	0.144	124.557	888.439	288.580
EPH_RE2B	0.947	0.947	0.946	0.942	0.898	0.819	0.737	0.679	0.668	0.531	0.141	112.662	761.008	246.810
LLZ_2ER	0.947	0.947	0.946	0.942	0.898	0.835	0.742	0.663	0.640	0.483	0.126	188.413	973.587	274.776
EPH_2ER	0.947	0.947	0.946	0.942	0.906	0.825	0.734	0.638	0.602	0.437	0.081	173.231	970.194	227.662

The conclusions from the second-day are not generally applicable to that garnered from the third day. In general, performances have been greatly enhanced with a TS larger than 0.8 for weaker rainfall (at smaller thresholds) which is rather common for widespread typhoon rainfall over the island. We have observed that the TSs are even larger than 0.5 for intense rainfall in some runs. For example, EPH produces a high TS up to 0.547 for 50-mm rainfall, which is highest among all the experiments except for EPH\_RE2A (0.554). Most of the assimilation experi-

ments exhibit considerably better performances for larger rainfall (above 20 mm) compared to the no-assimilation one (NONE). The impact of additional GTS data assimilation is not definitely positive or negative for all thresholds. On the other hand, adding a bogus vortex significantly degrades the performance for this day, as seen in TS from 0.789 (EPH) to 0.370 (EPH+TCBOG) or 0.828 (GTS+EPH) to 0.658 (GTS+EPH+TCBOG) for 10-mm rainfall. For this period, doubling the observation errors results in worse performance for larger rainfall assess-

ments (e.g., above 20 mm).

The above comparisons render the impact of different data assimilations on model performance rather diverse. For example, it might be expected that assimilation of additional GTS soundings should be more helpful than nothing, but the outcomes are not always supportive. Assimilation of a bogus vortex would provide a more intense typhoon depiction closer to observations, but it also exhibits no improvement due to larger track errors as seen in Fig. 12. Doubling the observation covariance errors also leads to worse performance for large rainfall. Thus, our proposed operator with the current defaults for the observation covariance errors (as inferred from Fig. 1) in WRF 3DVAR has presented a quite reasonable level of confidence for severe weather prediction. In this section, we present the gross exploration to show that the nonlocal operator is at least comparable to or better than the local operator. We do find that this new operator provides more improvement in the prediction of large or significant rainfall at later times than the local operator variant and the local operator. It will be of interest to understand how these impacts may be incurred in the following subsections.

#### 4.3 Influences Produced by the Nonlocal Operator

To explore why the simulation is improved with GPS RO assimilation by giving less precipitation over the island at later times than NONE, we looked into the differences (due to the assimilation) with the simulation time. Figure 14 shows the differences in water vapor mixing ratio at 3 km between EPH and NONE at 24 and 36 h. At the initial time, the increments show several impact zones at 3 km in height (also see Figs. 3 and 4). Over time, the impact zones have been widely transported and dispersed with positive and negative differences mainly produced in the east China and Taiwan area via typhoon circulation. The other two negative differences over east China have been dispersed with the flow along the northeast-southwest direction (Figs. 14a, b). The negative differences near the Philippines appear to follow the cyclonic vortex to merge with the increments near Taiwan. In order to better understand the impact of these GPS RO soundings by inspecting the trajectories of some particles released near the RO locations (Fig. 14c). As seen, only one of the released particles over one RO location was able to reach Taiwan as the mean flow dominates the particle's movement. However, particles adjacent to the RO locations (points 3, 4, and 7) may be transported into the target zone which is more influential for island rainfall (Fig. 14d). The contributions from points 3 and 7 should be more dominant since most of the trajectories get involved in the target zone. Particles released near point 7 are more likely to circle around east Taiwan. Since these trajectories are associated with mostly negative increments, the rainfall overprediction over the island may be abated in the EPH experiment.

#### 4.4 Sensitivity of Performances to Local RO Soundings

Although there are only seven RO observations in the outermost domain for this case, each sounding may play a different role in the local rainfall and circulation over the island. We are particularly interested in the effects of the two continental soundings over southeast China (points 6 and 7) and two oceanic soundings near the Philippines (points 3 and 4). As seen in Fig. 14c, the soundings, points 1, 2, 5, and 6, are too far away from the typhoon and thus may not have sizable influences on model prediction. The two experiments, EPH\_RE2A (absent the two oceanic soundings) and EPH\_RE2B (absent the two continental soundings), thus illustrate the differences from the performance of EPH with assimilation of all the seven points. Figure 15 shows the differences in the water vapor mixing ratio (in  $\text{g kg}^{-1}$ ) at 3 km height at 24 and 48 h between the two sensitivity tests and EPH. The differences between EPH\_RE2A and EPH (Figs. 15a, b) show major impact zones with much smaller magnitudes and scopes when compared to the differences between EPH\_RE2B and EPH (Figs. 15c, d). The contributions from the two continental soundings are more influential through the outer typhoon circulation as they may penetrate into southeast China to form two positive convergence bands at 48 h. Indeed, the TS increases and RMSE decreases (see Table 2) while keeping similar track performance for EPH\_RE2B when the two continental soundings are not used in EPH. Obviously, these remote soundings about 1000 ~ 1200 km away from Taiwan do play a significant role in rainfall activity over Taiwan. Although prediction of convective and orographic rainfall can be intimately influenced by many factors (e.g., model resolution, physical parameterization schemes, track errors, and vortex bogus-sing, etc.), it appears that the prediction of the accumulated rainfall is still improved when more realistic sounding information has been ingested to adjust the initial condition of the model.

### 5. CONCLUSIONS

In this study, we developed a new operator for assimilation of the GPS RO refractivity soundings in WRF 3DVAR. This operator, called a nonlocal operator assimilates the integrated amount of refractivity along a straight ray path which is defined as an excess phase. For comparison, a local operator variant was developed in WRF 3DVAR. The local operator variant is equivalent to the nonlocal operator, except that for the former, the length of integration is limited near the RO point. The performance of the default local operator in WRF 3DVAR was also investigated in this study. In providing observation error covariances used in WRF 3DVAR, observation errors for both local and nonlocal operator were evaluated based on WRF daily weather

predictions of the Asian region during the summer. Statistics indicate that the observation errors for the nonlocal operator are about two times smaller than those for the local operator and in agreement with Sokolovskiy et al. (2005b).

Here we should note that in our study both a nonlocal operator and local operator variant with smear tangent points are performed on the mean height of each model level (with 31 levels in all), while the local operator is performed with tangent points (fixed by the perigee point) at the observation

level (usually about 200 levels).

To assess the potential impact of GPS RO soundings on model prediction, we employ the WRF model (version 2.1.2) to simulate Typhoon Kaemi (July 2006) which struck Taiwan with torrential rainfall. In order to understand the sole impact of the GPS RO data, we leave the typhoon unmodified by not bogussing an intense vortex into the model in most of the experiments conducted in this study. A bogus vortex routinely implemented in the operational typhoon

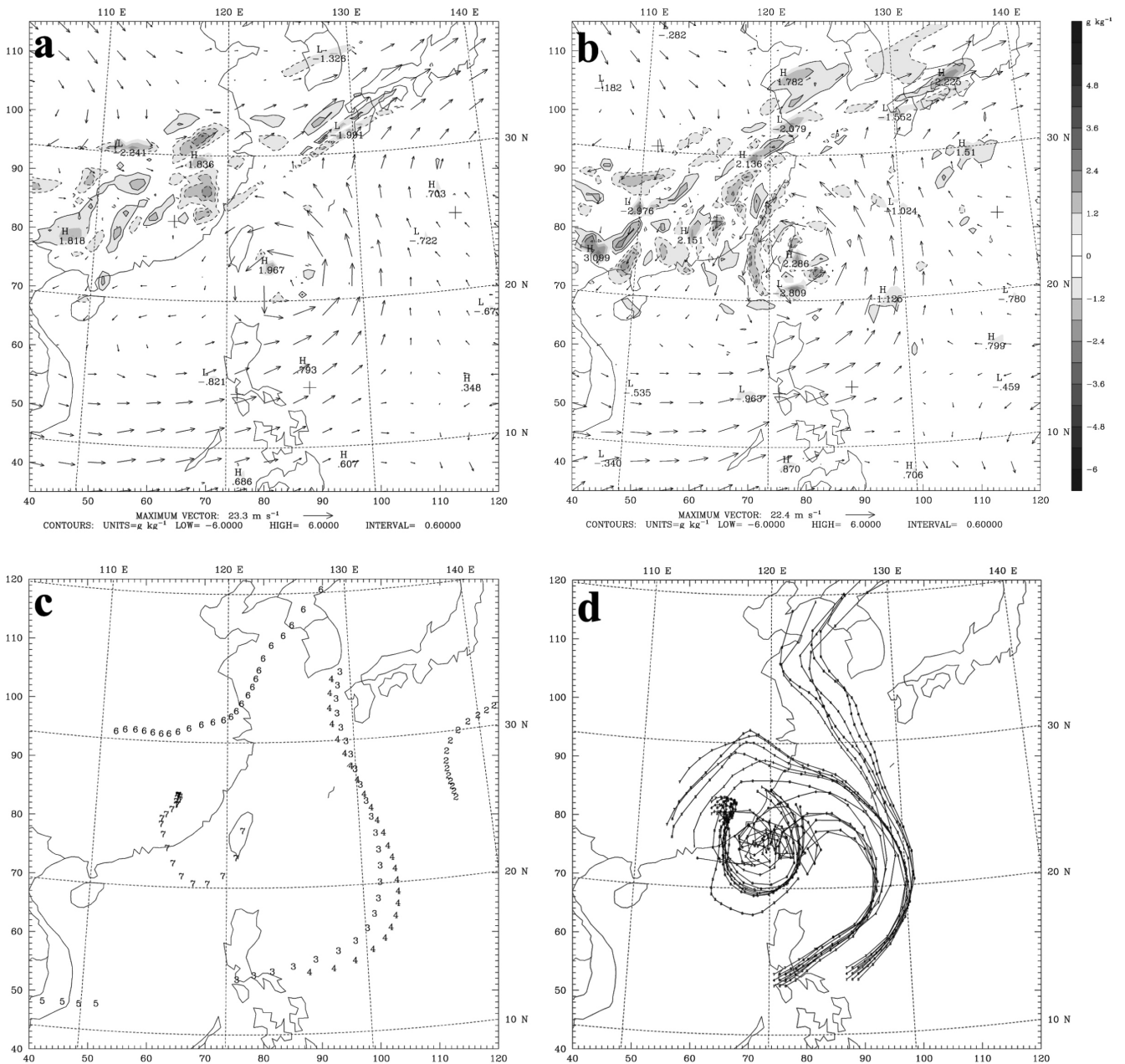


Fig. 14. The differences of the water vapor mixing ratio ( $\text{g kg}^{-1}$ ) in domain 1 at 3-km height between experiments EPH and NONE (EPH-NONE) at (a) 24 h and (b) 36 h. The wind vectors ( $\text{m s}^{-1}$ ) at the same time and height for experiment EPH are overlapped. The locations of GPS RO events are marked by plus signs. (c) The trajectories of the seven particles released at the locations of the seven GPS RO soundings at 3-km height for EPH as indicated by the numbers for the points and (d) the trajectories of nine particles released at 500 m height near GPS RO points 3, 4, and 7 for experiment EPH.

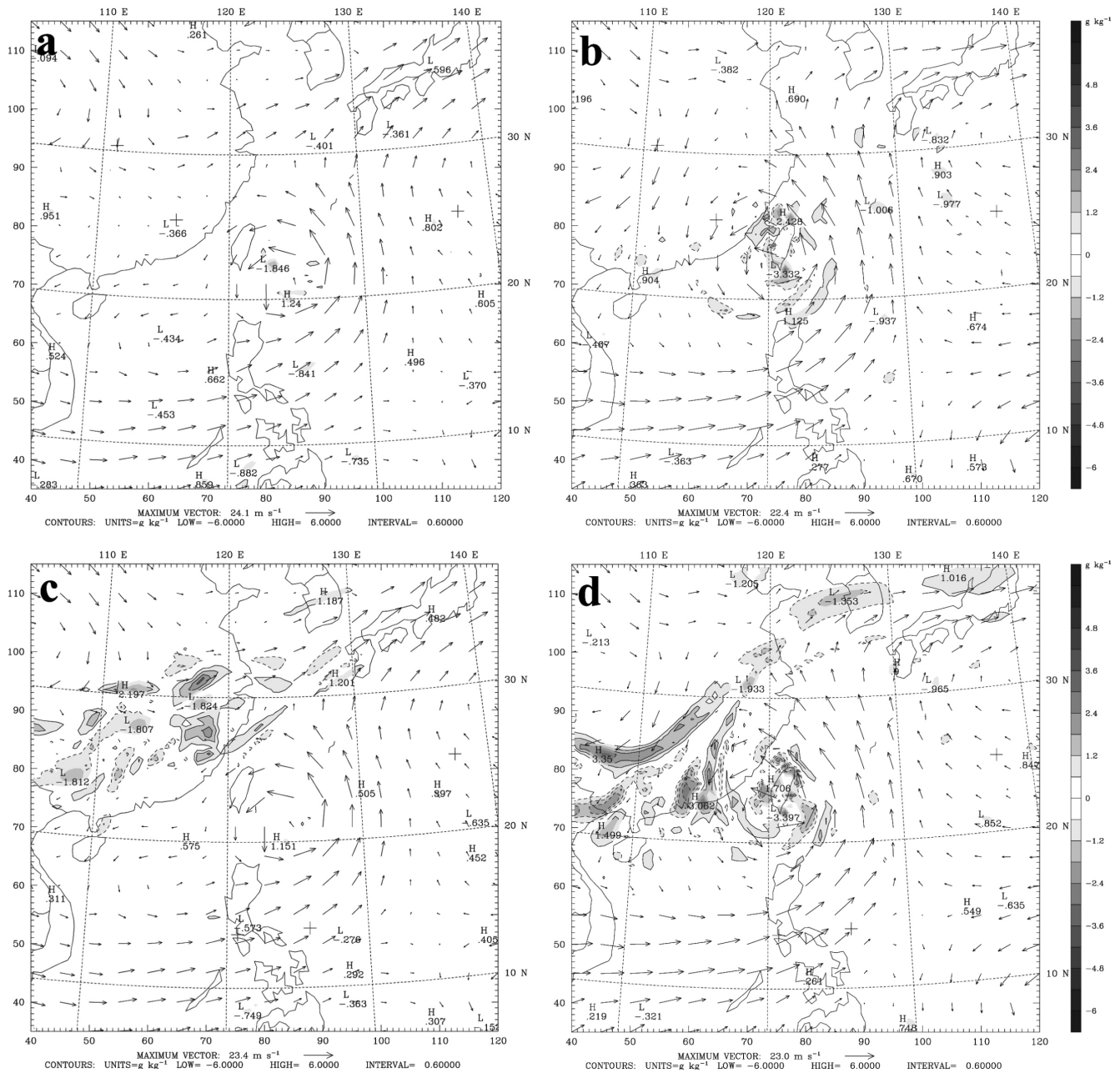


Fig. 15. The differences of the water vapor mixing ratio ( $\text{g kg}^{-1}$ ) in domain 1 at 3-km height between experiments EPH\_RE2A and EPH at (a) 24 h and (b) 48 h, and the wind vectors ( $\text{m s}^{-1}$ ) at the same time and height for EPH\_RE2A are overlapped. (c) and (d) as in (a) and (b), respectively, but for the differences between EPH\_RE2B and EPH, and overlapped the wind vectors for EPH\_RE2B.

model at CWB has also been assimilated as “observations” for a sensitivity study.

Assimilation of seven GPS RO refractivity soundings available from FORMOSAT-3/COSMIC for this case indicates that initial increments produced by both the nonlocal operator and local operator variant are quite similar in horizontal and vertical distributions. The modifications from the nonlocal operator, however, show slight ellipticity along the ray’s direction, as a result of the integration effect. In a predictive run without GPS data assimilation, the track of the

typhoon is well known by the second day before making landfall in southeast Taiwan while the simulated track has deviated somewhat with a southward bias over the last day. Both the local operator variant and the nonlocal operator give similar performances of a typhoon tracking prediction, which are better than that for the local operator. Overprediction of the accumulated rainfall during landfall in the third day of the run without the assimilation has also been reduced by assimilation of GPS RO refractivity. Verification against best tracks and rainfall observations over Tai-

wan indicates that the nonlocal operator can simulate typhoon tracking quite well and also better predict latter rainfall patterns compared to the two local operators.

Other sensitivity tests on inclusions of GTS soundings, vortex bogussing and removal of particular soundings were also conducted and the model performances were compared with their counterparts. The two oceanic GPS soundings near the Philippines and the two continental soundings in east China give diverse impacts on predictions of both the tracking and rainfall over Taiwan. Objective evaluations tend to indicate that the oceanic GPS soundings are more influential to later rainfall prediction as the typhoon vortex closes on Taiwan. In addition, assimilation of GTS soundings may be helpful for model prediction but a positive impact does not always hold for larger rainfall. Further, including vortex bogussing is not particularly beneficial for improving the prediction in this study although it gives an initial stronger vortex.

A nonlocal operator in principle is more accurate than a local operator as found in statistical observational error analyses in this study and Sokolovskiy et al. (2005a, b). Our assimilation study with the nonlocal operator has shown some promising results for one typhoon event when compared to the performance of a local operator. Assimilation of GPS RO refractivity may particularly improve the initial environmental analysis on moisture and temperature, which may lead to better model prediction. This nonlocal operator was developed herein primarily for a better representativeness of the Abel-retrieved refractivity test and it is less complicated in formulation, more effective in computation and more easily treated in regional models as compared to bending-angle assimilation. This study presents feasible and meaningful advances in providing an effective tool in WRF 3DVAR for assimilating abundant GPS RO soundings available from FORMOSAT-3/COSMIC.

**Acknowledgements** This study was supported by the National Science Council in Taiwan under the Grants NSC 95-2911-M-008-004-AP1 and by the National Space Program Organization in Taiwan under Grants 95-NSPO(B)-RS3-FA07-01. Partial support for the two-year visit of the first author by NCAR is greatly appreciated.

## REFERENCES

- Anthes, R. A., C. Rocken, and Y. H. Kuo, 2000: Applications of COSMIC to meteorology and climate. *Terr. Atmos. Ocean. Sci.*, **11**, 115-156.
- Barker, D., W. Huang, Y. R. Guo, and A. Bourgeois, 2003: A three-dimensional variational (3DVAR) data assimilation system for use with MM5. NCAR Technical Note NCAR/TN-453+STR, 68 pp.
- Barker, D., W. Huang, Y. R. Guo, A. J. Bourgeois, and Q. N. Xiao, 2004: A three-dimensional variational data assimilation system for MM5: Implementation and initial results. *Mon. Wea. Rev.*, **132**, 897-914, doi: 10.1175/1520-0493(2004)132<0897:ATVDAS>2.0.CO;2. [[Link](#)]
- Chen, S. H., F. Vandenberghe, and C. Y. Huang, 2006: Error characteristics of GPS retrieved refractivity using a simulation study. *J. Meteorol. Soc. Jpn.*, **84**, 477-496, doi: 10.2151/jmsj.84.477. [[Link](#)]
- Cucurull, L., Y. H. Kuo, D. Barker, and S. R. H. Rizvi, 2006: Assessing the impact of simulated COSMIC GPS radio occultation data on weather analysis over the Antarctic: A case study. *Mon. Wea. Rev.*, **134**, 3283-3296, doi: 10.1175/MWR3241.1. [[Link](#)]
- Healy, S. B. and J. N. Thepaut, 2006: Assimilation experiments with CHAMP GPS radio occultation measurements. *Q. J. R. Meteorol. Soc.*, **132**, 605-623, doi: 10.1256/qj.04.182. [[Link](#)]
- Healy, S. B., A. M. Jupp, and C. Marquardt, 2005: Forecast impact experiment with GPS radio occultation measurements. *Geophys. Res. Lett.*, **32**, L03804, doi: 10.1029/2004GL020806. [[Link](#)]
- Hollingsworth, A. and P. Lönnberg, 1986: The statistical structure of short-range forecast errors as determined from radiosonde data. Part I: The wind field. *Tellus*, **38A**, 111-136.
- Huang, C. Y., Y. H. Kuo, S. H. Chen, and F. Vandenberghe, 2005: Improvements on typhoon forecast with assimilated GPS occultation refractivity. *Weather Forecast.*, **20**, 931-953, doi: 10.1175/WAF874.1. [[Link](#)]
- Kuo, Y. H., X. Zou, and W. Huang, 1997: The impact of GPS data on the prediction of an extratropical cyclone: An observing system simulation experiment. *Dyn. Atmos. Oceans*, **27**, 439-470, doi: 10.1016/S0377-0265(97)00023-7. [[Link](#)]
- Kuo, Y. H., S. V. Sokolovskiy, R. A. Anthes, and F. Vandenberghe, 2000: Assimilation of GPS radio occultation data for numerical weather prediction. *Terr. Atmos. Ocean. Sci.*, **11**, 157-186.
- Kuo, Y. H., T. K. Wee, S. Sokolovskiy, C. Rocken, W. Schreiner, D. Hunt, and R. A. Anthes, 2004: Inversion and error estimation of GPS radio occultation data. *J. Meteorol. Soc. Jpn.*, **82**, 507-531, doi: 10.2151/jmsj.2004.507. [[Link](#)]
- Kuo, Y. H., W. S. Schreiner, J. Wang, D. L. Rossiter, and Y. Zhang, 2005: Comparison of GPS radio occultation soundings with radiosondes. *Geophys. Res. Lett.*, **32**, L05817, doi: 10.1029/2004GL021443. [[Link](#)]
- Kursinski, E. R., G. A. Hajj, S. S. Leroy, and B. Herman, 2000: The GPS radio occultation technique. *Terr. Atmos. Ocean. Sci.*, **11**, 53-114.
- Liu, H. and X. Zou, 2003: Improvements to GPS radio occultation ray-tracing model and their impacts on assimilation of bending angle. *J. Geophys. Res.*, **108**, 4548, doi: 10.1029/2002JD003160. [[Link](#)]
- Ma, X. X., Y. R. Guo, Y. H. Kuo, and H. C. Lin, 2006: Observation error statistics of spaced-based GPS RO in WRF-Var system and numerical experiments for typhoon Djuan. The Seventh WRF Users' Workshop, P4.4., Boulder, Colorado.
- Poli, P., 2004: Effects of horizontal gradients on GPS radio

- occultation observation operators. II: A fast atmospheric refractivity gradient operator (FARGO). *Q. J. R. Meteorol. Soc.*, **130**, 2807-2825, doi: 10.1256/qj.03.229. [[Link](#)]
- Poli, P. and J. Joiner, 2004: Effects of horizontal gradients on GPS radio occultation observation operators. I: Ray tracing. *Q. J. R. Meteorol. Soc.*, **130**, 2787-2805, doi: 10.1256/qj.03.228. [[Link](#)]
- Rocken, C., R. Anthes, M. Exner, D. Hunt, S. Sokolovskiy, R. Ware, M. Gorbunov, W. Schreiner, D. Feng, B. Herman, Y. H. Kuo, and X. Zou, 1997: Analysis and validation of GPS/MET data in the neutral atmosphere. *J. Geophys. Res.*, **102**, 29849-29866, doi: 10.1029/97JD02400. [[Link](#)]
- Skamarock, W. C., J. B. Klemp, J. Dudhia, D. O. Gill, D. M. Barker, W. Wang, and J. G. Powers, 2005: A description of the advanced research WRF version 2. NCAR technical note NCAR/TN-468+STR, 100 pp.
- Sokolovskiy, S., Y. H. Kuo, and W. Wang, 2005a: Assessing the accuracy of linearized observation operator for assimilation of the Abel-retrieved refractivity: Case simulation with high-resolution weather model. *Mon. Wea. Rev.*, **133**, 2200-2212, doi: 10.1175/MWR2948.1. [[Link](#)]
- Sokolovskiy, S., Y. H. Kuo, and W. Wang, 2005b: Evaluation of a linear phase observation operator with CHAMP radio occultation data and high-resolution regional analysis. *Mon. Wea. Rev.*, **133**, 3053-3059, doi: 10.1175/MWR3006.1. [[Link](#)]
- Wu, W. S., R. J. Purser, and D. F. Parrish, 2002: Three-dimensional variational analysis with spatially inhomogeneous covariance. *Mon. Wea. Rev.*, **130**, 2905-2916, doi: 10.1175/1520-0493(2002)130<2905:TDVAWS>2.0.CO;2. [[Link](#)]
- Zou, X. and Q. Xiao, 2000: Studies on the initialization and simulation of a mature hurricane using a variational bogus data assimilation scheme. *J. Atmos. Sci.*, **57**, 836-860, doi: 10.1175/1520-0469(2000)057<0836:SOTIAS>2.0.CO;2. [[Link](#)]
- Zou, X., F. Vandenberghe, B. Wang, M. E. Gorbunov, Y. H. Kuo, S. Sokolovskiy, J. C. Chang, J. G. Sela, and R. Anthes, 1999: A ray-tracing operator and its adjoint for the use of GPS/MET refraction angle measurements. *J. Geophys. Res.*, **104**, 22301-22318, doi: 10.1029/1999JD 900450. [[Link](#)]
- Zou, X., B. Wang, H. Liu, R. A. Anthes, T. Matsumura, and Y. J. Zhu, 2000: Use of GPS/MET refraction angles in 3D variational analysis. *Q. J. R. Meteorol. Soc.*, **126**, 3013-3040, doi: 10.1002/qj.49712657003. [[Link](#)]